USING NATURAL WAVELET BASES AND MULTISCALE STOCHASTIC MODELS FOR TOMOGRAPHIC RECONSTRUCTION

M. Bhatia, W. C. Karl, and A. S. Willsky *

Stochastic Systems Group
Laboratory for Information and Decision Systems
Massachusetts Institute of Technology
Cambridge, Massachusetts 02139
Telephone: (617) 253-3816 Telefax: (617) 258-8553
Email: <mbhatia@athena.mit.edu>

Laboratory for Information and Decision Systems, MIT, Technical Report LIDS-P-2196

Abstract

We use a multiscale natural pixel type representation of an object, originally developed for incomplete data problems, to construct nearly orthonormal basis functions. The coefficients of expansion of an object in these basis functions are obtained as the 1-D wavelet transform of the (strip integral) projections of the object. This enables us to formulate a multiscale tomographic reconstruction technique wherein the object is reconstructed at multiple scales or resolutions. A complete reconstruction is obtained by combining the reconstructions at different scales. The nearly orthonormal behavior of the basis functions results in a system matrix, relating the input (the object coefficients) and the output (the projection data), which is extremely sparse. The system matrix, in addition to being sparse, is well-conditioned and has a symmetric block-Toeplitz structure if the angular projections are uniformly spaced between 0^0 and 180^0. Fast inversion algorithms exist for these matrices. The multiscale reconstruction technique can find applications in object feature recognition directly from projection data, tackling ill-posed imaging problems where the projection data are incomplete and/or noisy, and construction of multiscale stochastic models for which fast estimation algorithms exist. In this paper, we include examples illustrating the above applications of our multiscale reconstruction technique.

---

*This work was supported by the Office of Naval Research under grant N00014-91-J-1004, by the US Army Research Office under grant DAAL03-92-G-0115, and by the Air Force Office of Scientific Research under grant F49620-92-J-0002.

Report Documentation Page

Form Approved
OMB No. 0704-0188

1. REPORT DATE **1993**	2. REPORT TYPE	3. DATES COVERED **00-00-1993 to 00-00-1993**

4. TITLE AND SUBTITLE **Using Natural Wavelet Bases and Multiscale Stochastic Models for Tomographic Reconstruction**	5a. CONTRACT NUMBER 5b. GRANT NUMBER 5c. PROGRAM ELEMENT NUMBER
6. AUTHOR(S)	5d. PROJECT NUMBER 5e. TASK NUMBER 5f. WORK UNIT NUMBER
7. PERFORMING ORGANIZATION NAME(S) AND ADDRESS(ES) **Massachusetts Institute of Technology,Laboratory for Information and Decision Systems,77 Massachusetts Avenue,Cambridge,MA,02139-4307**	8. PERFORMING ORGANIZATION REPORT NUMBER
9. SPONSORING/MONITORING AGENCY NAME(S) AND ADDRESS(ES)	10. SPONSOR/MONITOR'S ACRONYM(S) 11. SPONSOR/MONITOR'S REPORT NUMBER(S)

12. DISTRIBUTION/AVAILABILITY STATEMENT
Approved for public release; distribution unlimited

13. SUPPLEMENTARY NOTES

14. ABSTRACT

15. SUBJECT TERMS

16. SECURITY CLASSIFICATION OF:			17. LIMITATION OF ABSTRACT	18. NUMBER OF PAGES	19a. NAME OF RESPONSIBLE PERSON
a. REPORT **unclassified**	b. ABSTRACT **unclassified**	c. THIS PAGE **unclassified**		**35**	

Standard Form 298 (Rev. 8-98)
Prescribed by ANSI Std Z39-18

1 Introduction

The conventional, and most commonly used, method for image reconstruction from tomographic projections is a *transform method* called *Convolution Back-Projection* (CBP) [1]. The CBP reconstruction, though fast, is not suitable for imaging problems where the projection data are incomplete (limited angle and/or truncated projections) [2, 7] or noisy and where the fundamental interest is not in the actual pixel values themselves, but rather in something that is derived from these, such as averages, boundaries [4] etc. These problems are encountered in many applications in medicine, non-destructive testing, oceanography and surveillance. Here we present a transform method for image reconstruction where we work in a multiscale transform space. This multiscale reconstruction method provides a framework that has the potential of overcoming the above limitations of the CBP reconstruction. Specifically, we use a natural pixel type representation of an object [5, 6] to construct nearly orthonormal basis functions. The coefficients of expansion of the object in these basis functions can be computed from the projection (i.e. the strip integral) data by using the wavelet transform.

The natural pixel method [5, 6] expands the object in the same basis functions along which the projection data are collected, thereby using a basis representation for the object that is closer to the measurement domain than the standard rectangular pixel basis. The natural pixel representation results in a matrix based reconstruction method. Since matrix based reconstruction methods do not utilize the space invariance assumption of the CBP, the natural pixel reconstruction is devoid of the many limited data artifacts present in the CBP reconstruction. The disadvantage of the natural pixel reconstruction, or the matrix based reconstruction methods in general, is that inversion of very large, ill-conditioned matrices is required.

In this paper, we build on the natural pixel approach by using wavelet bases to transform the natural pixel basis functions. The use of the wavelet bases enables us to formulate a multiscale tomographic reconstruction technique wherein *the object is reconstructed at multiple scales or resolutions.* The coarser scales contain the low frequency (i.e. the low resolution) information about the reconstructed object and the finer scales contain the high frequency (i.e. the high resolution) information. The standard reconstruction is obtained by combining the reconstructions at different scales. The natural pixel transformation matrix, relating the input (the object coefficients) and the output (the projection data), is *full.* The use of wavelet bases, in addition to providing a multiscale framework, results in this transformation matrix being *sparse.* Also, the multiscale framework allows us to use simple geometric arguments to partition the multiscale transformation matrix such that the reconstruction method requires only the inversion of a sparse and well-conditioned matrix which is symmetric block-Toeplitz if the projections are uniformly spaced between 0^0 and 180^0. Note that fast inversion algorithms exist for these matrices.

Many imaging problems are ill-posed in the sense that we wish to reconstruct more degrees of freedom than exist in the data. Noisy and/or incomplete projections (as in low dose medical imaging, oceanography, and in several applications of nondestructive testing of materials) make the reconstruction problem ill-posed. In these problems the lower resolution (i.e. the coarser scale) reconstructions are more reliable than their higher resolution counterparts. The multiscale reconstruction approach provides estimates of the field (or the object) at a variety of resolutions thus providing a natural framework for explicitly assessing the *resolution-accuracy tradeoff.* We show, through examples, that for an ill-posed reconstruction problem, some regularization can be achieved by only combining coarser scale reconstructions instead of reconstructions at all the scales. For noisy data problems, we specialize our multiscale reconstruction method to yield fast MAP multiscale reconstruction estimates corresponding to a chosen prior on the multiscale object coefficients.

Apart from this, the multiscale framework is useful in many other situations. It lends itself naturally to situations where the projection data are collected at multiple resolutions. It also provides the *ability to reconstruct different parts of the object at different resolutions*. This could be particularly useful, for example, if the projection data is gathered with spatially varying density or if the desire is to focus computational resources at certain points of interest.

Finally, the multiscale reconstruction method provides a means of *object feature extraction directly from the projection data*. For instance, if we are only interested in imaging high frequency details within the object (for example, boundaries[1]), then we could directly obtain these features by using only the finer scale information in the data. Similarly, if averages[2] of the pixel values in a region are desired, then only the coarser scale information is needed. Using conventional, ad hoc techniques, we would first have to reconstruct the object and then use post-processing to extract such features. The disadvantages of the conventional approach are that (a) a good quality reconstruction (and hence a complete projection data set) is required for post-processing [4], and (b) even though the noise in projection measurements is white, the noise in the reconstructed image is colored, and hence the necessity of using a 2-D whitening filter on the reconstructed image [3].

The paper is organized as follows. In Section 2 we describe the tomographic reconstruction problem. In Section 3 we describe the natural pixel reconstruction technique and explore it's relationship with conventional reconstruction methods. In Section 4, starting from the natural pixel object representation, we develop the theory behind our multiscale reconstruction method. We present some sample reconstructions in Section 5, and present conclusions in Section 6. Appendices 1-5 contain mathematical details of our multiscale reconstruction method, and Appendix 6 summarizes the mathematical notations used throughout this paper.

2 The Tomographic Reconstruction Problem

In non-diffraction tomography, the goal is to reconstruct an object or a field, f, from the projection data [1]. For a parallel-beam imaging geometry, the projection data consists of parallel, non-overlapping strip integrals through the object at various angles (refer to Figure 1). Each angular position corresponds to a specific source-detector orientation. Thus the projection data can be mathematically represented as y_{kn}, where $k = 1, \ldots, M$ (M is the number of uniformly spaced angular positions between 0 and 180^0), and $n = 1, \ldots, N$ (N is the number of parallel strip integrals in each angular position). Furthermore, we call ϕ_{kn} the indicator function of the strip labeled by

---

[1] Boundary detection has applications in medical imaging (detection and outlining of boundaries of organs and tumors), nondestructive testing, oceanography and plant physiological studies [4].

[2] Computation of average values in a region of the field has applications in functional medical imaging.

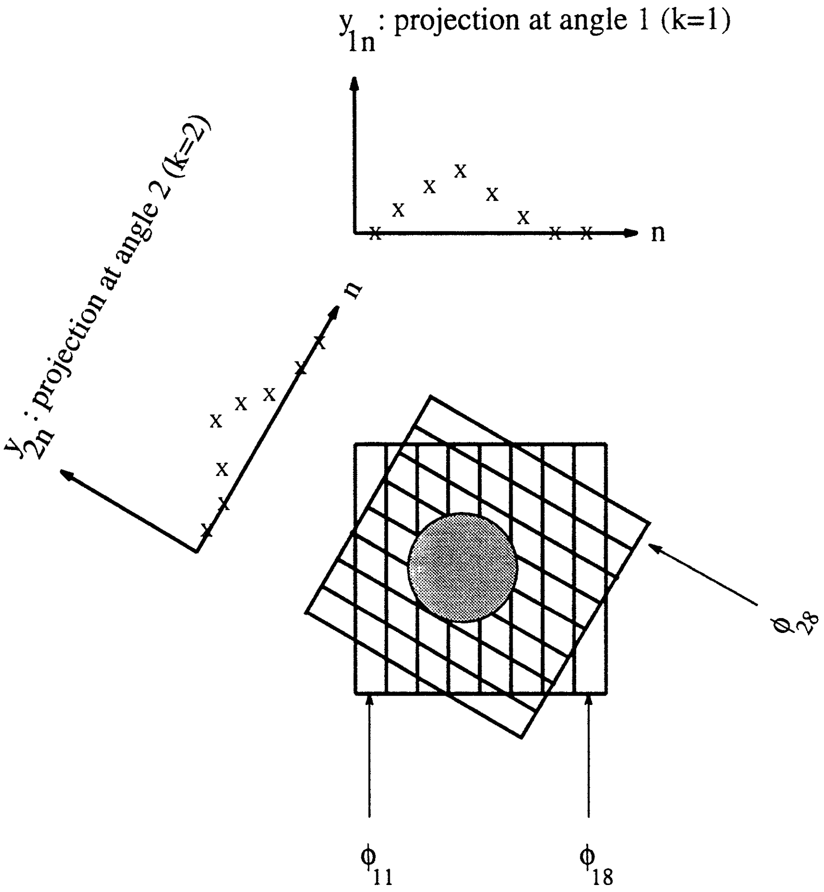

Figure 1: The projection measurements for an object, f (shaded), at two different angular positions ($k = 1$ and $k = 2$ respectively). The number of parallel strip integrals in each angular projection, N, is 8 in this case. Three basis functions, $\phi_{11}, \phi_{18}, \phi_{28}$, which are the indicator functions of the corresponding strips, are also shown.

(k, n) so that ϕ_{kn} has value one within that strip and zero otherwise. Given this notation,

$$y_{kn} = \iint_{\Omega} f(u,v)\, \phi_{kn}(u,v)\, du\, dv \qquad k = 1, \ldots, M; \qquad n = 1, \ldots, N \tag{1}$$

where (u, v) are the rectangular coordinates and the integration is carried over a region of interest Ω.

Due to practical considerations, we have to work with a discretized version of Equation 1. This is

$$\underline{y} = \left[\ \underline{y}^T(1)\ \ \underline{y}^T(2)\ \ \ldots\ \ \underline{y}^T(k)\ \ \ldots\ \ \underline{y}^T(M)\ \right]^T = \phi \underline{f} \tag{2}$$

where $\underline{y}(k)$ is the projection data set collected at angle k, and is composed of the N strip integrals as shown below

$$\underline{y}(k) = \begin{bmatrix} y_{k1} & y_{k2} & \cdots & y_{kN} \end{bmatrix}^T. \tag{3}$$

The vector $\underline{f}$ is formed by first discretizing $f(u,v)$ on a rectangular lattice (we will assume a $p \times p$ square pixel lattice) and then stacking the discretized values in a lexicographic order into a vector

$$\underline{f} = \begin{bmatrix} f_1 & f_2 & \cdots & f_{p^2} \end{bmatrix}^T \tag{4}$$

and the $MN \times p^2$ matrix ϕ is formed by first stacking all $\{\phi_{kn}(u,v),\ \ k = 1,\ldots,M;\ \ n = 1,\ldots,N\}$ into a vector followed by discretization in u and v (on the same square pixel lattice used for f) and lexicographic ordering (to match that in f)

$$\phi = \begin{bmatrix} \underline{\phi}_{11}^T \\ \underline{\phi}_{12}^T \\ \vdots \\ \underline{\phi}_{MN}^T \end{bmatrix} = \begin{bmatrix} \phi_{11,1} & \phi_{11,2} & \cdots & \phi_{11,p^2} \\ \phi_{12,1} & \phi_{12,2} & \cdots & \phi_{12,p^2} \\ \vdots & \vdots & \vdots & \vdots \\ \phi_{MN,1} & \phi_{MN,2} & \cdots & \phi_{MN,p^2} \end{bmatrix}. \tag{5}$$

The tomographic reconstruction problem then reduces to finding an estimate, $\hat{\underline{f}}$, of the discretized object, $\underline{f}$, given the projection data $\underline{y}$.

3 The Conventional Reconstruction Techniques

In this section we discuss two conventional reconstruction techniques, the widely used convolution back-projection (CBP) reconstruction technique, and the natural pixel (NP) reconstruction technique used by us as a starting point for our multiscale reconstruction.

In both the CBP and the NP reconstructions, the object is represented as a linear combination of (non-orthogonal) basis functions ϕ along which the projection data are collected. Mathematically,

$$\hat{f}(u,v) = \sum_{k=1}^{M} \sum_{n=1}^{N} x_{kn}\, \phi_{kn}(u,v). \tag{6}$$

The discretized version of the above equation is

$$\hat{\underline{f}} = \phi^T \underline{x} \tag{7}$$

where

$$\underline{x} = \begin{bmatrix} \underline{x}^T(1) & \underline{x}^T(2) & \cdots & \underline{x}^T(k) & \cdots & \underline{x}^T(M) \end{bmatrix}^T. \tag{8}$$

In the above equation, $\underline{x}(k)$ is the object coefficient set at angle k, and is composed of the N object coefficients as shown below

$$\underline{x}(k) = \begin{bmatrix} x_{k1} & x_{k2} & \cdots & x_{kN} \end{bmatrix}^T. \tag{9}$$

In the NP reconstruction, the coefficients of expansion, x_{kn}, are called the *natural pixels*. Equation 7 can also be interpreted as the back-projection operation where the coefficients x_{kn} are back-projected along the basis functions ϕ_{kn}. Thus if the natural pixels, x_{kn}, are the same as the ramp-filtered projection coefficients of the CBP, the natural pixel and the CBP reconstructions will give identical results. We will come back to this later.

3.1 The convolution back-projection (CBP) reconstruction

The CBP reconstruction assumes a *space-invariant* point spread function [7, 8, 9] and hence is only valid for *complete data* problems. We borrow the definition of a complete data set from Llacer. According to Llacer [7], "a complete data set could be described as sufficient number of line projections at a sufficient number of angular increments such that enough independent measurements are made to allow the image reconstruction of a complete bound region."

In the CBP reconstruction, the space invariance property is utilized to calculate $\underline{x}(k)$ at each angular position, k, by convolving the projection data at that particular angular position with the inverse Fourier transform of a ramp filter [1]. Thus, for a fixed angular position k,

$$\begin{aligned} \underline{x}(k) &= F^{-1}(\underline{\rho}) * \underline{y}(k) \\ &= T_a\, \underline{y}(k) \end{aligned} \tag{10}$$

where $\underline{\rho}$ is a vector containing the 1-D ramp filter coefficients, $F^{-1}(\underline{\rho})$ represents the 1-D inverse fourier transform of the 1-D ramp filter, $*$ refers to 1-D convolution in the spatial domain, and the matrix T_a performs the operation $F^{-1}(\underline{\rho})*$. Let

$$T = I_{M\times M} \otimes T_a \tag{11}$$

where $I_{M\times M}$ is an $M \times M$ identity matrix and $\otimes$ refers to the Kronecker product. The above equation implies that T is a block-diagonal matrix with M blocks along the diagonal, all equal to T_a. Thus, for the CBP reconstruction, the necessary steps are as follows[3] (a) computation of the basis coefficients $\underline{x}$ from projection data $\underline{y}$ by the equation

$$\underline{x} = T\underline{y} \tag{12}$$

where T is as defined in Equation 11, and (b) back-projection according to

$$\underline{\hat{f}} = \phi^T \underline{x} = \phi^T T \underline{y}. \tag{13}$$

Note that if all elements of $\underline{\rho}$ are replaced by unity, then Equation 13 reduces to simple back-projection reconstruction (without any filtering). This reconstruction is approximately equal to the true object, $f(r,\theta)$ in radial coordinates, blurred with a (circularly symmetric) $1/r$ point spread function.

3.2 The natural pixel (NP) reconstruction

In the NP reconstruction [5, 6], the space-invariance assumption of the point spread function is not used to find the natural pixels, $\underline{x}$, from the projection data, $\underline{y}$, and hence it's applicability to incomplete data problems. Equations 2 and 7 are used instead. Thus the CBP reconstruction can be viewed as a special case of the NP reconstruction under space-invariance or complete data assumptions. By substituting $\hat{f}$ from Equation 7 for f in Equation 2, we get

$$\underline{y} = (\phi\phi^T)\underline{x} = G\underline{x} \qquad \text{where } G = \phi\phi^T. \tag{14}$$

---

[3] In practice, for ***regularization purposes***, a ***roll-off*** is applied to the ramp filter. This operation would include an additional matrix Q and so $F^{-1}(\underline{\rho})$ will be replaced by $F^{-1}(Q\underline{\rho})$ [1].

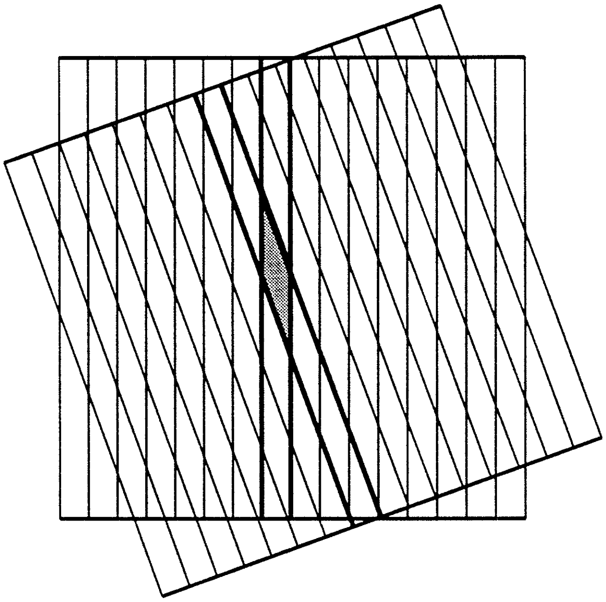

Figure 2: The elements of the matrix G are the areas of intersection of various strips. One such area of intersection, corresponding to two strips delineated by bold lines, is shown shaded. The matrix G is full as most of these areas are non-zero.

The elements of the matrix G are the areas of intersection of the strips defined by the basis functions ϕ. Most of these areas are not zero and hence the matrix G is *full* (refer to Figure 2). It can be easily shown that G is symmetric block-Toeplitz if the M angular projections are uniformly spaced between 0^0 and 180^0, even though G may be quite ill-conditioned in general, as we will see later. Figure 7, top, shows G for an imaging geometry with 32 angular projections (i.e. $M = 32$) and with 32 strip integrals (i.e. $N = 32$) in each angular projection.

The *advantage* of the NP reconstruction over the CBP reconstruction is that (a) since the matrix G can be calculated or measured for each specific geometry, the reconstruction can be customized for any imaging system, and (b) the point spread function does not have to be space invariant and hence a complete set of angular projection data is not required as in CBP. However, the NP reconstruction suffers from some *disadvantages* as well, namely that (a) the large size of the matrix G ($MN \times MN$) imposes a limitation on storage and speed, and (b) the matrix G can be quite ill-conditioned for some imaging geometries (see the following discussion and [7, 8, 9]).

In the next section, we use wavelet bases to transform the NP basis functions, ϕ, into the multiscale framework. As described in the Introduction, we gain many important features in going to the multiscale framework. In addition, we overcome the above limitations of the NP reconstruction. The multiscale system matrix, Γ_θ, is related to G by a similarity transformation and is sparse. This and the fact that Γ_θ is block-Toeplitz for the case of uniformly spaced angular projections, offsets the first disadvantage of the NP reconstruction. Also, the geometry of the imaging system is naturally captured in Γ_θ. We exploit this feature to partition Γ_θ into well and ill-conditioned matrices such that our reconstruction procedure requires inversion of only well-conditioned matrices. This offsets the second disadvantage of the NP reconstruction.

Connection with the least-squares reconstruction

If the matrix ϕ has full row rank, then the NP matrix G is invertible and in this case the NP solution is given by $\underline{\hat{f}} = \phi^T G^{-1} \underline{y}$. This is just a special case of the minimum 2-norm least squares solution to $y = \phi f$ (Equation 2) and given by [12]

$$\underline{\hat{f}}_{LS} = \phi^+ \underline{y} \tag{15}$$

where ϕ^+ refers to the *pseudo-inverse* of ϕ. However, as we discuss next, it is not possible in general to invert G even when ϕ has full row rank. This is because the matrix G is ill-conditioned due to the inherent non-uniqueness in the NP representation.

Non-uniqueness in the NP representation

Because the NP object representation is tied to the collection of projection data, there is an inherent non-uniqueness in the representation which results in G not having full rank or being badly conditioned. Specifically, $G = \phi\phi^T$ has full rank (i.e. is invertible) if and only if ϕ has full row rank. Recall from Equation 5 that the rows of ϕ are composed of discretized basis functions, $\underline{\phi}_{11}^T, \ldots, \underline{\phi}_{kn}^T, \ldots, \underline{\phi}_{MN}^T$. Thus G has full rank if none of these basis functions can be written as a linear combination of the others. This is not true if two disjoint subsets of $\{\underline{\phi}_{kn}\}$ span the same object subspace. As an example, assume that all angular projection sets exactly span the entire object space. Then obviously

$$\sum_{n=1}^{N} \underline{\phi}_{k_1 n} - \sum_{n=1}^{N} \underline{\phi}_{k_2 n} = \underline{0} \quad \forall\ k_1 \neq k_2, \text{ and } k_1, k_2 = 1, \ldots, M \tag{16}$$

because the DC term in the object appears in all M angular projections. Thus, in this example, ϕ does not have full row rank, resulting in a singular G. Throughout this paper, we assume that $p = N$ (i.e. the object is discretized in a $p \times p = N \times N$ rectangular pixel lattice, where N = number of strip integrals in each angular projection) and that the M angular projections are uniformly spaced between 0 and 180^0. Thus ϕ and G are $MN \times MN$ square matrices. In this geometry, Equation 16 is true only if k_1 and k_2 correspond to projections at 0^0 and 90^0, since only projections at these angles exactly span the entire object space. Now, angular projections at 0^0 and 90^0 exist if and only if M is even because of our assumption of uniformly spaced angular projections. Thus if M is even, ϕ has rank $MN - 1$, otherwise it has a full rank of MN. Similarly, it can be shown that G drops a rank for each pair of projections 90^0 apart. There are projection pairs 90^0 apart if and only if M is even, in which case there are exactly $M/2$ of them. Thus if M is even, G has a rank of $MN - M/2$, otherwise it has a full rank of MN.

Thus, if M is even, it is not possible to uniquely solve for $\underline{x}$ in $\underline{y} = G\underline{x}$. Because of numerical issues (we use 7 digit precision for calculation of elements of G), the matrix G has full rank for even as well as odd M. The condition number is a good measure to use in this case. In Figure 3, we show the condition numbers of G for imaging geometry with $M = N$ and for values of M ranging from 8 to 18. Notice the steep fluctuation in condition numbers between odd and even values of M, and the steady increase of the condition number for increasingly odd values of M. This is

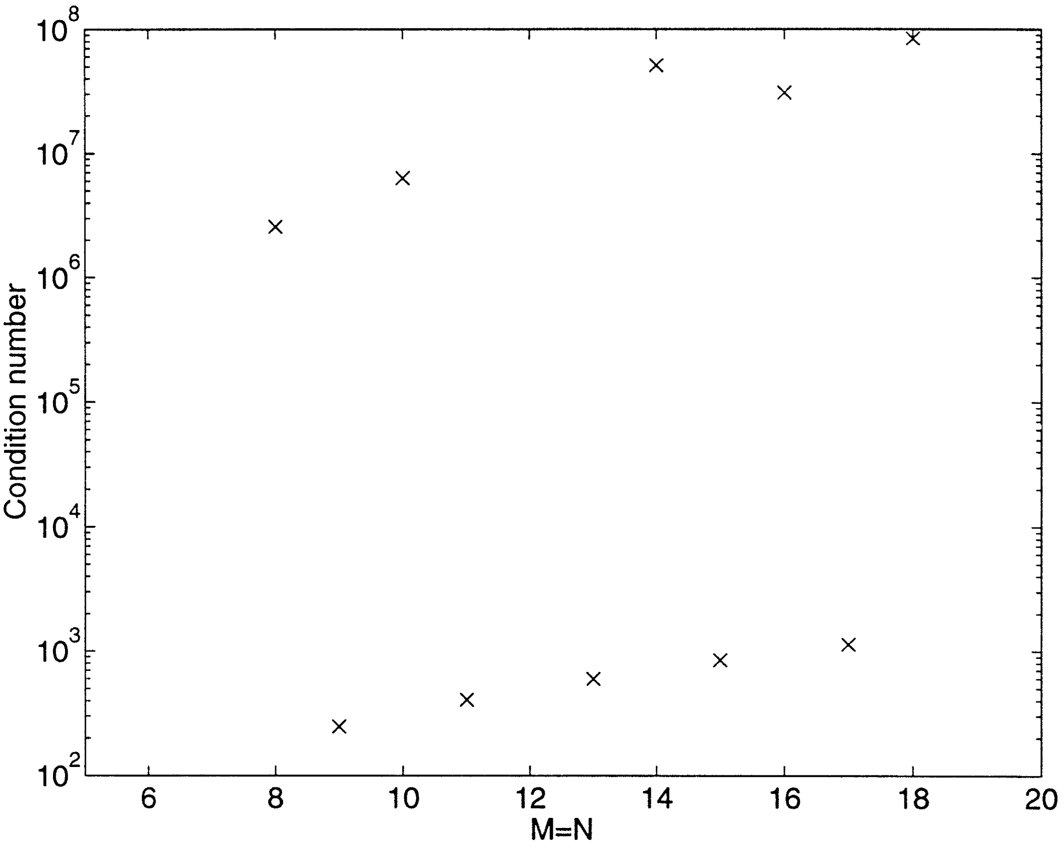

Figure 3: The condition number of G as a function of $M = N$.

because projection pairs approach being 90^0 apart as M is increased in this case. Thus, due to this ill-conditioning, it is not possible to uniquely solve for $\underline{x}$ in $\underline{y} = G\underline{x}$ even for odd values of M. We show, in Section 4, that this non-uniqueness problem of the NP representation is easily dealt with in the multiscale framework. As a result, the system matrix in the multiscale framework can be partitioned into well and ill-conditioned matrices such that the reconstruction requires inversion of only well-conditioned matrices.

The dropping of the rank of G for each projection angle pair 90^0 apart is illustrated in Figure 4. For simplicity, consider a 2×2 object

$$\underline{f} = \begin{bmatrix} f_1 & f_2 & f_3 & f_4 \end{bmatrix}^T \tag{17}$$

and projection measurements

$$\begin{aligned} \underline{y} &= \begin{bmatrix} y_{11} & y_{12} & y_{21} & y_{22} \end{bmatrix}^T & (18) \\ &= \begin{bmatrix} f_1 + f_3 & f_2 + f_4 & f_1 + f_2 & f_3 + f_4 \end{bmatrix}^T . & (19) \end{aligned}$$

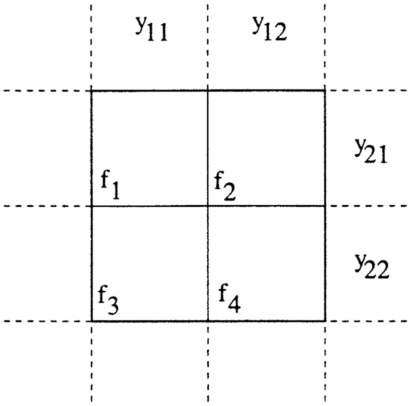

Figure 4: Imaging geometry where the object, f, is discretized on a $p^2 = 4$ pixel lattice. Here $M = N = 2$ with the projections being 90^0 apart.

Here

$$\phi = \begin{bmatrix} 1 & 0 & 1 & 0 \\ 0 & 1 & 0 & 1 \\ 1 & 1 & 0 & 0 \\ 0 & 0 & 1 & 1 \end{bmatrix} \tag{20}$$

has a rank of 3, and

$$G = \phi\phi^T = \begin{bmatrix} 2 & 0 & 1 & 1 \\ 0 & 2 & 1 & 1 \\ 1 & 1 & 2 & 0 \\ 1 & 1 & 0 & 2 \end{bmatrix} \tag{21}$$

also has a rank of 3.

4 The Multiscale Reconstruction

The multiscale reconstruction is motivated by the following observations. In the previous section we saw that the NP reconstruction involves solving for the natural pixels, $\underline{x}$, from the projection data, $\underline{y}$, which are related by $\underline{y} = G\underline{x}$ and then back-projecting $\underline{x}$, $\underline{\hat{f}} = \phi^T \underline{x}$. Also, the elements of matrix G are the areas of intersection of the various strips along which the projection data are collected. Suppose now that the strips are of the form shown in Figure 5. Each strip is a linear combination of two NP strips, one given a positive weight and the other negative. The new matrix relating x and y, according to the above choice of strips, will have as its elements the areas of intersections of the newly defined strips. It is clear from Figure 5 that most of these elements will be zero due to the cancellation of the positive and the negative terms. Only those elements that correspond to strip intersections near the edge of the field-of-view will be non-zero. Thus one can expect this new matrix to be *sparse* with the degree of sparsity increasing with the size of the field-of-view.

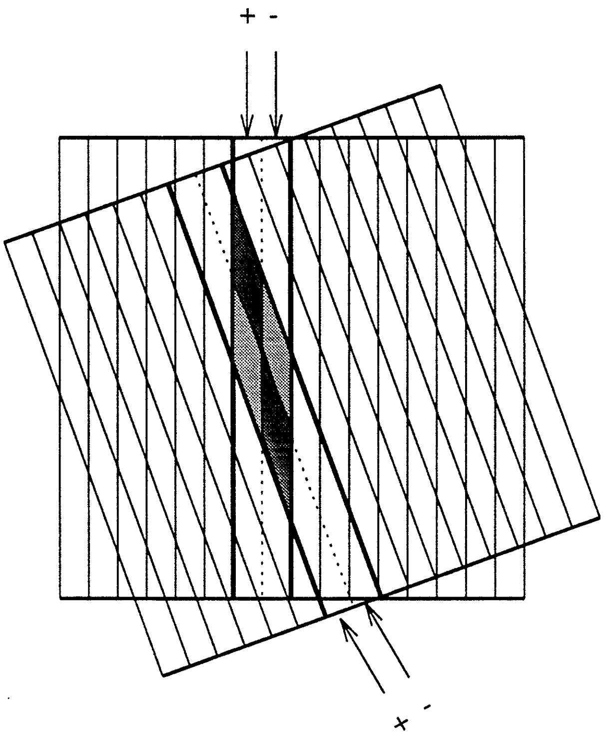

Figure 5: Each of the two delineated strips from figure 2 are broken down into two substrips, having a positive and a negative weight respectively. The area of intersection of the two strips is zero in this case due to the cancellation of the positive (lightly shaded) and the negative (darkly shaded) terms.

The above redefinition of the strips with positive and negative weights is reminiscent of the finest scale contribution from the Haar transform. However, an important point to note here is that the Haar transform is taken only in one direction, i.e. the direction perpendicular to the long axis of the strip. As an example, for a projection at a fixed angle, $k = 1$, and consisting of eight strips (i.e. $N = 8$), the full Haar transform will look as shown in Figure 6. A notion of scale emerges from the use of the Haar transform. The original strips have been broken down into strips at multiple scales having positive and negative weights. The finest scale involves strips that have twice the width of the original strips and the coarsest scale involves strips that have eight times the width of the original strips. We will call the above transformation of the strips the *natural wavelet transform* because of the adaptation to the natural pixel representation.

Let the new strips be defined by the basis functions $\{\underline{\Phi}_{ksn}\}$ (recall that the original strips were defined by basis functions $\{\underline{\phi}_{kn}\}$). We use lowercase for the original NP basis functions and uppercase for the multiscale basis functions. Note that each multiscale basis function $\underline{\Phi}_{ksn}$ is labeled by three subscripts, ksn, where k indicates the angle of the projection ($k = 1, \ldots, M$), s indicates the scale ($s = 1, 2, \ldots, 1 + \ln N/\ln 2$; $N = 2^i$, $i \in Z^+$), and n indicates the shift within the scale ($n = 1, 2, \ldots, n_s$; $n_s = N/2^s$ for $s = 1, 2, \ldots, \ln N/\ln 2$ and $n_s = 1$ for $s = 1 + \ln N/\ln 2$). In the future, we will refer to the finest scale ($s = 1$) as h (for *h̲igh*), the coarsest scale ($s = \ln N/\ln 2$) as

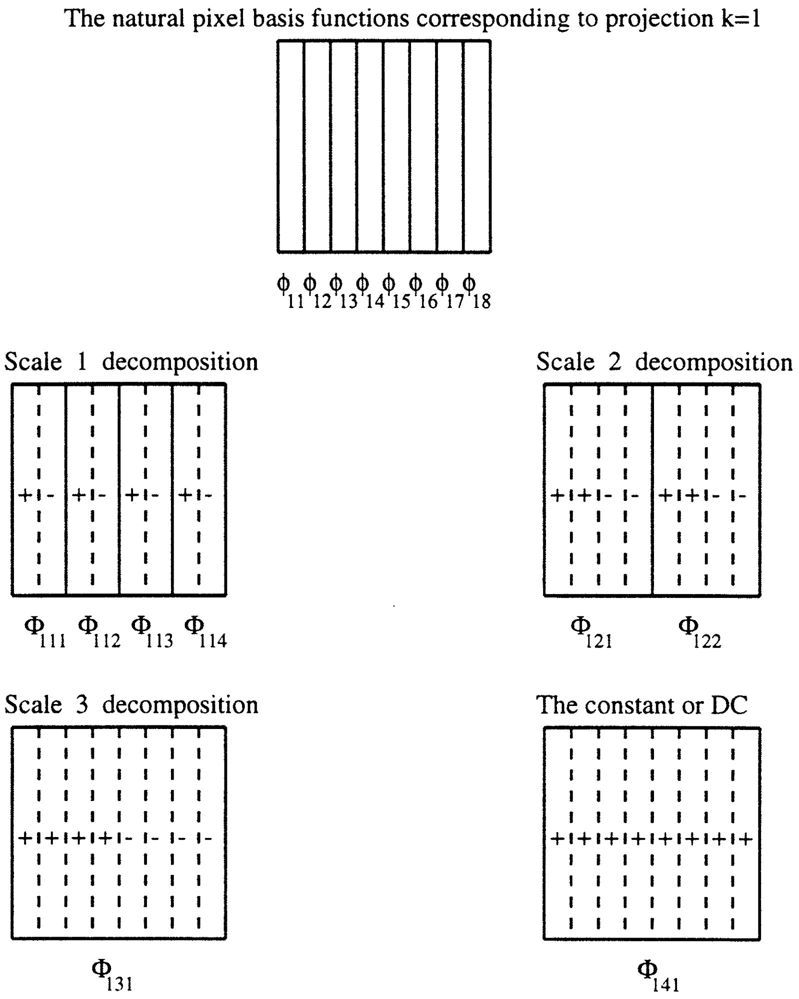
The natural pixel basis functions corresponding to projection k=1

Scale 1 decomposition

Scale 2 decomposition

Scale 3 decomposition

The constant or DC

Figure 6: The basis functions $\{\phi_{1n}\}$ (or equivalently the strips defined by them) are decomposed into functions at multiple scales given by $\{\Phi_{1sn}\}$.

l (for low), and the DC component ($s = 1 + \ln N / \ln 2$) as d (for dc). Thus $s = h, h+1, \ldots, l, d$.

Let W_a be a matrix representation of the linear operator that performs a 1-D orthogonal wavelet decomposition on a discrete sequence[4]. Then, at a fixed angular position k, our new multiscale

---

[4] We use the Discrete Periodic Wavelet Transform (DPWT) [11] with the Haar and the various Daubechies compactly supported wavelets [10] for our reconstructions. A Daubechies compactly supported wavelet D_m is characterized by m vanishing moments.

basis functions and the previous NP basis functions are related by

$$\left[\begin{array}{c} \underline{\Phi}_{kh1}^T \\ \vdots \\ \underline{\Phi}_{khn_h}^T \\ \hline \vdots \\ \vdots \\ \hline \underline{\Phi}_{kl1}^T \\ \vdots \\ \underline{\Phi}_{kln_l}^T \\ \hline \underline{\Phi}_{kd1}^T \end{array}\right] = W_a \left[\begin{array}{c} \underline{\phi}_{k1}^T \\ \underline{\phi}_{k2}^T \\ \vdots \\ \vdots \\ \vdots \\ \vdots \\ \vdots \\ \underline{\phi}_{kN}^T \end{array}\right] \tag{22}$$

with $W_a^{-1} = NW_a^T$ because of our choice of orthogonal wavelet basis normalized such that the absolute values of elements in the multiscale counterpart of matrix G lie between 0 and 1 irrespective of the size of the imaging system. As an example, for $N = 8$ and using the Haar basis (Figure 6), the bases at a single angle are related by

$$\left[\begin{array}{c} \underline{\Phi}_{k11}^T \\ \underline{\Phi}_{k12}^T \\ \underline{\Phi}_{k13}^T \\ \underline{\Phi}_{k14}^T \\ \hline \underline{\Phi}_{k21}^T \\ \underline{\Phi}_{k22}^T \\ \hline \underline{\Phi}_{k31}^T \\ \hline \underline{\Phi}_{k41}^T \end{array}\right] = W_a \left[\begin{array}{c} \underline{\phi}_{k1}^T \\ \underline{\phi}_{k2}^T \\ \underline{\phi}_{k3}^T \\ \underline{\phi}_{k4}^T \\ \underline{\phi}_{k5}^T \\ \underline{\phi}_{k6}^T \\ \underline{\phi}_{k7}^T \\ \underline{\phi}_{k8}^T \end{array}\right] \tag{23}$$

where

$$W_a = \frac{1}{4}\left[\begin{array}{cccccccc} 1 & -1 & 0 & 0 & 0 & 0 & 0 & 0 \\ 0 & 0 & 1 & -1 & 0 & 0 & 0 & 0 \\ 0 & 0 & 0 & 0 & 1 & -1 & 0 & 0 \\ 0 & 0 & 0 & 0 & 0 & 0 & 1 & -1 \\ \hline \frac{1}{\sqrt{2}} & \frac{1}{\sqrt{2}} & -\frac{1}{\sqrt{2}} & -\frac{1}{\sqrt{2}} & 0 & 0 & 0 & 0 \\ 0 & 0 & 0 & 0 & \frac{1}{\sqrt{2}} & \frac{1}{\sqrt{2}} & -\frac{1}{\sqrt{2}} & -\frac{1}{\sqrt{2}} \\ \hline \frac{1}{\sqrt{4}} & \frac{1}{\sqrt{4}} & \frac{1}{\sqrt{4}} & \frac{1}{\sqrt{4}} & -\frac{1}{\sqrt{4}} & -\frac{1}{\sqrt{4}} & -\frac{1}{\sqrt{4}} & -\frac{1}{\sqrt{4}} \\ \hline \frac{1}{\sqrt{4}} & \frac{1}{\sqrt{4}} & \frac{1}{\sqrt{4}} & \frac{1}{\sqrt{4}} & \frac{1}{\sqrt{4}} & \frac{1}{\sqrt{4}} & \frac{1}{\sqrt{4}} & \frac{1}{\sqrt{4}} \end{array}\right]. \tag{24}$$

Let

$$W = I_{M\times M} \otimes W_a \tag{25}$$

i.e. W is a block-diagonal matrix with M blocks along the diagonal, all equal to W_a. Then

$$\underline{\Phi} = W\underline{\phi} \tag{26}$$

with $W^{-1} = NW^T$, where

$$\underline{\Phi} = \left[\begin{array}{ccccccccccc} \underline{\Phi}_{1h1} & \cdots & \underline{\Phi}_{1d1} & \cdots\cdots & \underline{\Phi}_{kh1} & \cdots & \underline{\Phi}_{kd1} & \cdots\cdots & \underline{\Phi}_{Mh1} & \cdots & \underline{\Phi}_{Md1} \end{array}\right]^T \tag{27}$$

and ϕ is as defined in Equation 5.

Recall the natural pixel equations (2), (7) and (14). The multiscale decomposition of vectors $\underline{x}$ and $\underline{y}$, given by $\underline{\xi}_\theta$ and $\underline{\psi}_\theta$ respectively, is defined as

$$\underline{\xi}_\theta \triangleq NW\underline{x} \tag{28}$$

and

$$\underline{\psi}_\theta \triangleq W\underline{y} \tag{29}$$

where we use the subscript θ to indicate ordering according to projection angles corresponding to our choice of W in Equation 25. Thus, to illustrate θ ordering,

$$\underline{\psi}_\theta = \left[\begin{array}{ccccccc} \underline{\psi}_\theta^T(1) & \underline{\psi}_\theta^T(2) & \ldots & \underline{\psi}_\theta^T(k) & \ldots & \underline{\psi}_\theta^T(M) \end{array} \right]^T \tag{30}$$

where $\underline{\psi}_\theta(k)$ is the 1-D wavelet transform of the projection data set at angle k, $\underline{y}(k)$, and is composed of the elements at different scales as shown below

$$\underline{\psi}_\theta(k) = W_a\underline{y}(k) = \left[\begin{array}{ccccccc} \underline{\psi}_\theta^T(k,h) & \underline{\psi}_\theta^T(k,h+1) & \ldots & \underline{\psi}_\theta^T(k,j) & \ldots & \underline{\psi}_\theta^T(k,d) \end{array} \right]^T. \tag{31}$$

In the above, $\underline{\psi}_\theta(k,j)$ is the vector containing the jth scale components of the 1-D wavelet transform of $\underline{y}(k)$

$$\underline{\psi}_\theta(k,j) = \left[\begin{array}{cccc} \psi_{kj1} & \psi_{kj2} & \ldots & \psi_{kjn_j} \end{array} \right]^T \tag{32}$$

with

$$n_j = \left\{ \begin{array}{ll} \frac{N}{2^j} & \text{for } j \neq d \\ 1 & \text{for } j = d. \end{array} \right. \tag{33}$$

Similarly

$$\underline{\xi}_\theta = \left[\begin{array}{ccccccc} \underline{\xi}_\theta^T(1) & \underline{\xi}_\theta^T(2) & \ldots & \underline{\xi}_\theta^T(k) & \ldots & \underline{\xi}_\theta^T(M) \end{array} \right]^T \tag{34}$$

where $\underline{\xi}_\theta(k)$ is the 1-D wavelet transform of the object coefficient set at angle k, $\underline{x}(k)$, and is composed of the elements at different scales as shown below

$$\underline{\xi}_\theta(k) = NW_a\underline{x}(k) = \left[\begin{array}{ccccccc} \underline{\xi}_\theta^T(k,h) & \underline{\xi}_\theta^T(k,h+1) & \ldots & \underline{\xi}_\theta^T(k,j) & \ldots & \underline{\xi}_\theta^T(k,d) \end{array} \right]^T. \tag{35}$$

In the above, $\underline{\xi}_\theta(k,j)$ is the vector containing the jth scale components of the 1-D wavelet transform of $\underline{x}(k)$

$$\underline{\xi}_\theta(k,j) = \left[\begin{array}{cccc} \xi_{kj1} & \xi_{kj2} & \ldots & \xi_{kjn_j} \end{array} \right]^T \tag{36}$$

with

$$n_j = \left\{ \begin{array}{ll} \frac{N}{2^j} & \text{for } j \neq d \\ 1 & \text{for } j = d. \end{array} \right. \tag{37}$$

The three subscripts ksn, in ψ_{ksn} and ξ_{ksn} above, convey the same meaning and take on the same values as those for $\underline{\Phi}_{ksn}$.

In the multiscale coordinates, the input-output equation (14) changes to

$$\begin{array}{rcl} \underline{y} & = & G\underline{x} \\ W\underline{y} & = & WGW^{-1}W\underline{x} \\ \underline{\psi}_\theta & = & (WGW^T)\underline{\xi}_\theta \\ & = & \Gamma_\theta\underline{\xi}_\theta \end{array} \tag{38}$$

where the symmetric block-Toeplitz matrix Γ_θ is given by

$$\Gamma_\theta = WGW^T = W(\phi\phi^T)W^T = (W\phi)(W\phi)^T = \Phi\Phi^T. \tag{39}$$

The above equation implies that the elements of the matrix Γ_θ are the areas of intersection of the various multiscale basis functions Φ. We know from our earlier discussion that Γ_θ is *sparse*. The object representation equation (7) changes to

$$\begin{aligned} \hat{\underline{f}} &= \phi^T \underline{x} = \phi^T W^{-1} W \underline{x} = \phi^T W^T \underline{\xi}_\theta = (W\phi)^T \underline{\xi}_\theta \\ &= \Phi^T \underline{\xi}_\theta. \end{aligned} \tag{40}$$

In some cases it is more intuitive to order according to scales rather than projection angles. We will denote the scale ordering by subscript s. Thus

$$\underline{\psi}_s = P\underline{\psi}_\theta, \tag{41}$$

$$\underline{\xi}_s = P\underline{\xi}_\theta, \tag{42}$$

$$\underline{\psi}_s = \Gamma_s \underline{\xi}_s, \tag{43}$$

and

$$\Gamma_s = P\Gamma_\theta P^{-1} = P\Gamma_\theta P^T \tag{44}$$

where P is the (orthogonal) permutation matrix which changes projection angle ordering into scale ordering. Thus, to illustrate s ordering,

$$\underline{\psi}_s = \left[\begin{array}{ccccccc} \underline{\psi}_s^T(h) & \underline{\psi}_s^T(h+1) & \ldots & \underline{\psi}_s^T(j) & \ldots & \underline{\psi}_s^T(l) & \underline{\psi}_s^T(d) \end{array} \right]^T \tag{45}$$

where $\underline{\psi}_s(j)$ contains projection data at scale j from multiscale projection data sets at all angles and is given by

$$\underline{\psi}_s(j) = \left[\begin{array}{ccccccc} \underline{\psi}_\theta^T(1,j) & \underline{\psi}_\theta^T(2,j) & \ldots & \underline{\psi}_\theta^T(k,j) & \ldots & \underline{\psi}_\theta^T(M,j) \end{array} \right]^T. \tag{46}$$

Similarly

$$\underline{\xi}_s = \left[\begin{array}{ccccccc} \underline{\xi}_s^T(h) & \underline{\xi}_s^T(h+1) & \ldots & \underline{\xi}_s^T(j) & \ldots & \underline{\xi}_s^T(l) & \underline{\xi}_s^T(d) \end{array} \right]^T \tag{47}$$

where $\underline{\xi}_s(j)$ contains object coefficients at scale j from object coefficient sets at all angles and is given by

$$\underline{\xi}_s(j) = \left[\begin{array}{ccccccc} \underline{\xi}_\theta^T(1,j) & \underline{\xi}_\theta^T(2,j) & \ldots & \underline{\xi}_\theta^T(k,j) & \ldots & \underline{\xi}_\theta^T(M,j) \end{array} \right]^T. \tag{48}$$

As explained in the beginning of this section, we expect the multiscale matrices to be sparse. The number of non-zero elements in Γ_s and Γ_θ are the same and hence the degree of sparsity achieved in the multiscale framework can be studied using either of these. Figure 7, bottom, shows Γ_s for an imaging geometry with 32 angular projections (i.e. $M = 32$) and 32 strip integrals in each angular projection (i.e. $N = 32$). We have used the Haar wavelet for this multiscale representation. Comparing with Figure 7, top, which shows the corresponding NP system matrix, G, we see that Γ_s is sparser than G. From the figure, most of the non-zero terms in Γ_s correspond to the coarser scale terms where the edge effects are more pronounced. It was claimed in the previous section that Γ_s becomes more sparse as the size of the field-of-view increases. This claim is validated by Figure 8

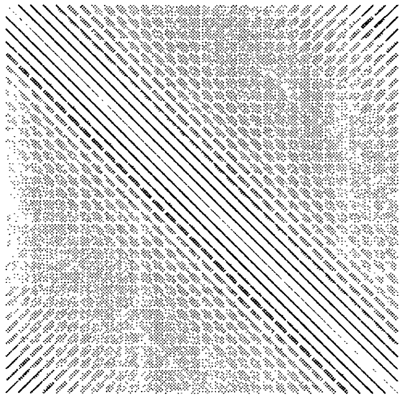

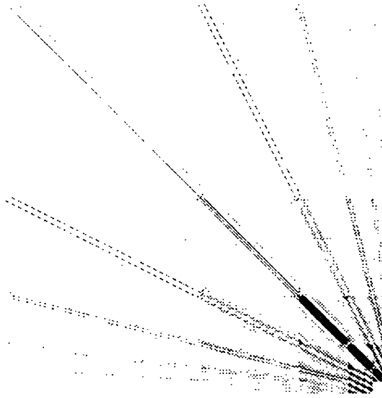

Figure 7: Top: Natural pixel system matrix, G; Bottom: Multiscale natural pixel system matrix, Γ_s, for an imaging geometry with 32 angular projections (i.e. $M = 32$) and with 32 strip integrals (i.e. $N = 32$) in each angular projection. The Haar wavelet is used for multiscale decomposition.

where we plot the degree of sparsity of Γ_s as a function of the parameter M ($= N$). We measure the degree of sparsity by the percentage of elements in matrix Γ_s which are below a certain threshold (the maximum value in Γ_s is normalized to 1). Figure 8 reports the sparsity calculations for three different values of threshold, namely 0, 0.005 and 0.02. It is empirically observed that setting all values in Γ_s below a threshold of 0.02 to zero, makes no visible difference to the reconstructions. From Figure 8, we see that for the case of $M = N = 128$ and a threshold of 0.02, Γ_s is 98.75% sparse (or, equivalently, 1.25% full). In Figure 9, we show the degree of sparsity of Γ_θ or Γ_s, for $M = N = 32$, achieved by the Haar wavelet, and the Daubechies wavelets D_3 and D_8. From the figure we see that the number of elements that are exactly zero decrease as wavelets with larger

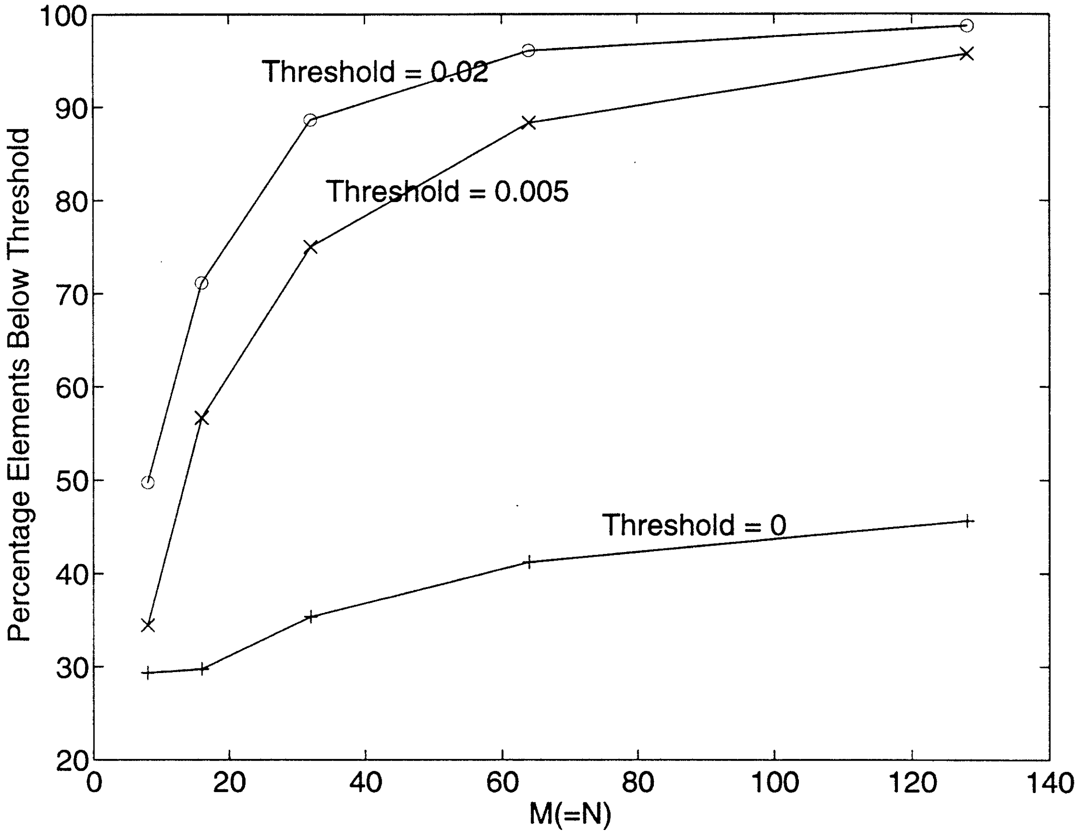

Figure 8: The degree of sparsity (percentage of elements below a threshold) of multiscale system matrix, Γ_s, as a function of M $(=N)$. The Haar wavelet is used here for multiscale decomposition. The maximum value in Γ_s is normalized to 1. Setting all elements in Γ_s below 0.02 to zero makes no visible difference to the reconstructions.

support are used. But, since we can always threshold all elements of the matrices below 0.005 to zero without affecting the reconstructions, the effective sparsity achieved by the Haar, D_3 and D_8 is approximately the same.

Next, we tackle the non-uniqueness issue of the NP representation. We had seen earlier that, with our assumption of $p = N$ (i.e. the object is discretized in a $p \times p = N \times N$ rectangular pixel lattice, where N = number of strip integrals in each angular projection) and M angular projections uniformly spaced between 0 and 180^0, G has a rank of $MN - M/2$ for M even and a (full) rank of MN for M odd. Γ_θ and Γ_s have the same rank as G. Thus, if M is even, it is not possible to uniquely solve for $\underline{\xi}_\theta(\underline{\xi}_s)$ in $\underline{\psi}_\theta = \Gamma_\theta \underline{\xi}_\theta(\underline{\psi}_s = \Gamma_s \underline{\xi}_s)$. We again consider the same 2×2 example as before (Figure 4). For this example, using the Haar basis,

$$\Gamma_s = \left[\begin{array}{cc|cc} 1 & 0 & 0 & 0 \\ 0 & 1 & 0 & 0 \\ \hline 0 & 0 & 1 & 1 \\ 0 & 0 & 1 & 1 \end{array}\right] \tag{49}$$

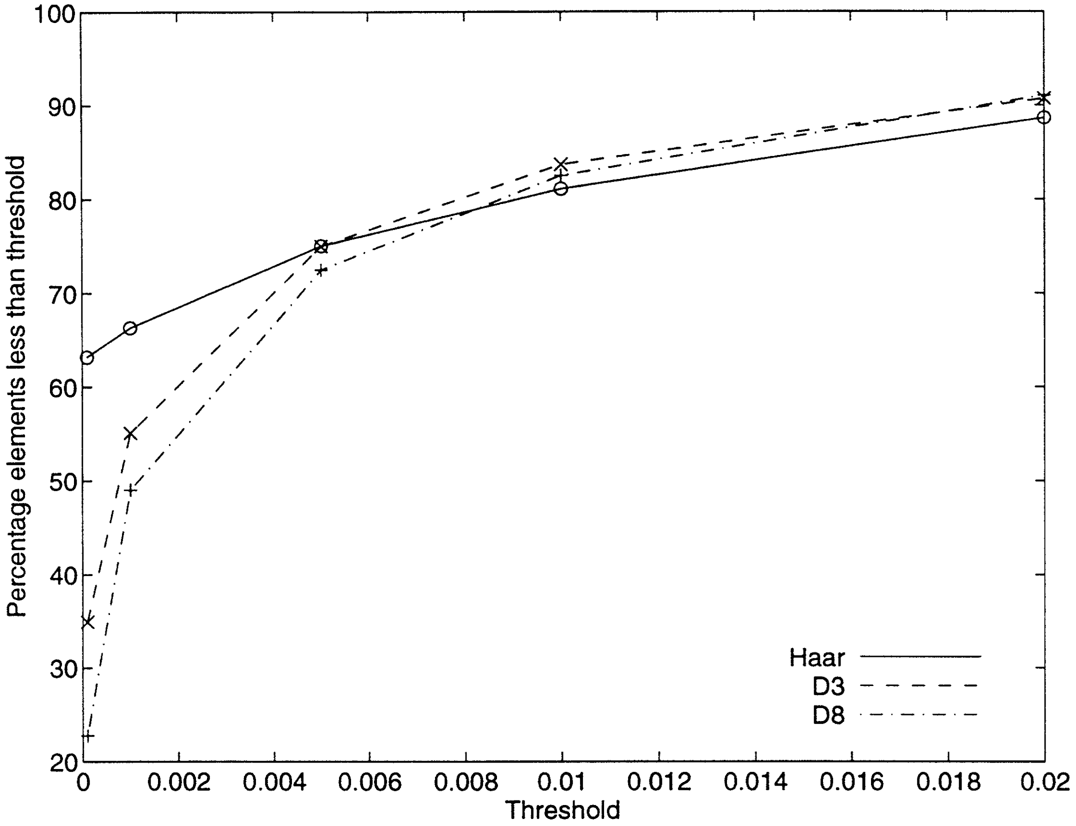

Figure 9: The degree of sparsity (percentage of elements below a threshold) of multiscale system matrix, Γ_s, as a function of threshold, for different wavelets. Here $M = N = 32$. The maximum value in Γ_s is normalized to 1. Setting all elements in Γ_s below 0.005 to zero makes no visible difference to the reconstructions.

has a rank of 3 because the two DC rows (and columns) corresponding to the two projections 90^0 apart are identical. In general for M projections, where M is even, $M/2$ of these rows and columns will be identical resulting in a $MN - M/2$ rank matrix. This suggests a recipe for partitioning Γ_s into ill and well-conditioned matrices. Taking advantage of this, we devise an approximation to the exact equation $\underline{\psi}_s = \Gamma_s \underline{\xi}_s$ which requires inversion of a relatively well-conditioned, full rank matrix. This approximate reconstruction is valid for all M, even or odd, and yields reconstructions which are almost identical to the CBP reconstruction for the complete data problem, and much better for the incomplete data case. We partition $\underline{\psi}_s = \Gamma_s \underline{\xi}_s$ according to

$$\left[\begin{array}{c}\underline{\psi}_{s-}\\ \hline \underline{\psi}_s(d)\end{array}\right] = \left[\begin{array}{c|c}\Gamma_{s1} & \Gamma_{s2}^T\\ \hline \Gamma_{s2} & \Gamma_{sd}\end{array}\right]\left[\begin{array}{c}\underline{\xi}_{s-}\\ \hline \underline{\xi}_s(d)\end{array}\right] \tag{50}$$

where Γ_{s1} is an $M(N-1) \times M(N-1)$ symmetric matrix, Γ_{s2} is an $M \times M(N-1)$ matrix, and Γ_{sd} is an $M \times M$ symmetric circulant matrix. The vectors $\underline{\psi}_s(d)$ and $\underline{\xi}_s(d)$ have length M and contain the DC terms. The vectors $\underline{\psi}_{s-}$ and $\underline{\xi}_{s-}$ have length $M(N-1)$ and are given by

$$\underline{\psi}_{s-} = \left[\ \underline{\psi}_s^T(h)\ \ \underline{\psi}_s^T(h+1)\ \ \ldots\ \ \underline{\psi}_s^T(j)\ \ \ldots\ \ \underline{\psi}_s^T(l)\ \right]^T \tag{51}$$

and

$$\underline{\xi}_{s-} = \left[\ \underline{\xi}_s^T(h)\ \ \underline{\xi}_s^T(h+1)\ \ \ldots\ \ \underline{\xi}_s^T(j)\ \ \ldots\ \ \underline{\xi}_s^T(l)\ \right]^T. \tag{52}$$

The $-$ in the subscript for $\underline{\psi}_{s-}$ and $\underline{\xi}_{s-}$ indicates that these vectors do not contain the DC terms.

As a consequence of using the DPWT, the DC (i.e. the last) row of matrices W_a and the DC basis functions $\underline{\Phi}_{kd1}$ are identical irrespective of the wavelet used. Thus, if we assume that the object is fully covered by all M projections, all M elements of $\underline{\psi}_s(d)$, which are the total number of counts in the corresponding angular projections, are equal irrespective of the wavelet used. Let the total number of counts be μ. Thus

$$\underline{\psi}_s(d) = \frac{\mu}{N}\underline{1}_M \tag{53}$$

where $\underline{1}_M$ refers to a vector of length M with all elements equal to unity.

As mentioned before, Γ_s is singular for even M. For odd M, Γ_s is invertible even though it may be quite ill-conditioned because of projection pairs nearly 90^0 apart. In both cases, M being even or odd, Γ_{s1} is well-conditioned. For even M, to overcome the problem of non-invertibility of Γ_s, we assume all M elements of the vector $\underline{\xi}_s(d)$ to be equal. Let this value be c. Then

$$\underline{\xi}_s(d) = c\underline{1}_M. \tag{54}$$

Thus

$$\left[\begin{array}{c} \underline{\psi}_{s-} \\ \hline \frac{\mu}{N}\underline{1}_M \end{array}\right] = \left[\begin{array}{c|c} \Gamma_{s1} & \Gamma_{s2}^T \\ \hline \Gamma_{s2} & \Gamma_{sd} \end{array}\right] \left[\begin{array}{c} \underline{\xi}_{s-} \\ \hline c\underline{1}_M \end{array}\right] \tag{55}$$

$$= \left[\begin{array}{c|c} \Gamma_{s1} & \underline{v} \\ \hline \Gamma_{s2} & \underline{u} \end{array}\right] \left[\begin{array}{c} \underline{\xi}_{s-} \\ \hline c \end{array}\right] \tag{56}$$

where $\underline{v}$ is a vector of length $M(N-1)$ the elements of which are the row sums of Γ_{s2}^T, and $\underline{u}$ is a vector of length M containing the row sums of Γ_{sd}. Now, the elements of matrix Γ_{sd} are the areas of intersection of basis function $\{\underline{\Phi}_{kd1};\ \ k = 1, \ldots, M\}$, and because of our assumption of uniformly spaced angles, Γ_{sd} is a *circulant* matrix (refer to Appendix 1). Thus the row sums of Γ_{sd}, and hence all M elements of vector $\underline{u}$, will be equal. Let this value be α. Thus

$$\underline{u} = \alpha\underline{1}_M. \tag{57}$$

Now, by manipulation of Equations 50 – 57 (refer to Appendix 2 for details), our multiscale reconstruction method consists of the following steps.

1. Form the matrix

$$\Gamma_s = \left[\begin{array}{c|c} \Gamma_{s1} & \Gamma_{s2}^T \\ \hline \Gamma_{s2} & \Gamma_{sd} \end{array}\right] = P\Gamma_\theta P^T = P(WGW^T)P^T \tag{58}$$

   which is sparse.

2. Transform the projection data in the multiscale basis

$$\underline{\psi}_s = \left[\begin{array}{c} \underline{\psi}_{s-} \\ \hline \underline{\psi}_s(d) \end{array}\right] = PW\underline{y}. \tag{59}$$

3. Calculate the multiscale natural pixels

$$\underline{\xi}_{s-} = A\underline{\psi}_{s-} + \underline{b} \tag{60}$$

where the constants A and $\underline{b}$ depend only on the parameters of the imaging system and the total counts in the object, and are given by

$$A = \Gamma_{s1}^{-1}(I - \frac{\underline{v}\underline{v}^T\Gamma_{s1}^{-1}}{\underline{v}^T\Gamma_{s1}^{-1}\underline{v} - \alpha M}) \tag{61}$$

and

$$\underline{b} = (\frac{\mu M}{N})(\frac{\Gamma_{s1}^{-1}\underline{v}}{\underline{v}^T\Gamma_{s1}^{-1}\underline{v} - \alpha M}). \tag{62}$$

Note that Equations 61 and 62 require the inverse of Γ_{s1} which is a full rank, relatively well-conditioned matrix[5]. The condition number of Γ_{s1}, using the Haar wavelet, for $M = N = 16$ is 209 and for $M = N = 32$, 1288. The condition number of Γ_s, on the other hand, is 3×10^7 and 1.4×10^5 respectively, for these two configurations. Also, since elements of $\underline{v}$ are mostly negligible (refer to Appendix 3), a good approximation to Equations 61 - 62 is

$$A \approx \Gamma_{s1}^{-1} \tag{63}$$

and

$$\underline{b} \approx \underline{0} \tag{64}$$

and thus

$$\underline{\xi}_{s-} \approx \Gamma_{s1}^{-1}\underline{\psi}_{s-}. \tag{65}$$

4. Back-project

$$\underline{\hat{f}} = \Phi_{s-}^T\underline{\xi}_{s-} + \frac{\mu}{N^2}\underline{1}_{N^2} \tag{66}$$

where

$$\Phi_s = \begin{bmatrix} \Phi_{s-} \\ \Phi_{sd} \end{bmatrix} = P\Phi. \tag{67}$$

To justify the above reconstruction algorithm for odd M, we have to simply justify the assumption that all M elements of $\underline{\xi}_s(d)$ are equal for odd M. This is done in Appendix 4.

To recapitulate, the multiscale reconstruction procedure as outlined above is based on the following two assumptions.

1. The elements of the matrix Γ_{s2} are mostly negligible. This is empirically seen to be true for the Haar and the compactly supported Daubechies wavelets. In Appendix 3, we demonstrate the validity of this assumption in the Haar case by calculating numerical bounds on the absolute values of the elements of Γ_{s2}.
2. All M (DC) elements of $\underline{\xi}_s(d)$ are equal if the object is entirely covered by all M projections. We show, in Appendix 4, that this assumption is exactly true when Γ_s has full rank, i.e. when M is odd, irrespective of the wavelet used.

---

[5] If Γ_{s1} is rearranged according to projection angles, the resulting matrix is symmetric block-Toeplitz.

4.1 Specialization for noisy projection data

The noisy projection data is represented as

$$\underline{y} = \phi \underline{f} + \underline{n} \tag{68}$$

where $\underline{n}$ is the noise vector which we model as zero-mean, white and Gaussian with variance λ'. Thus $\underline{n} \sim N(\underline{0}, \lambda' I_{MN \times MN})$. This results in the input-output equation (compare with Equation 43)

$$\underline{\psi}_s = \Gamma_s \underline{\xi}_s + \underline{\nu}_s \tag{69}$$

where

$$\underline{\nu}_s = PW\underline{n}. \tag{70}$$

Since P is an orthogonal matrix and $W^{-1} = NW^T$, $\underline{\nu} \sim N(\underline{0}, \lambda I_{MN \times MN})$ where

$$\lambda = \frac{\lambda'}{N}. \tag{71}$$

As before, we can partition Equation 69 as (compare with Equation 50)

$$\left[\begin{array}{c} \underline{\psi}_{s-} \\ \hline \underline{\psi}_s(d) \end{array}\right] = \left[\begin{array}{c|c} \Gamma_{s1} & \Gamma_{s2}^T \\ \hline \Gamma_{s2} & \Gamma_{sd} \end{array}\right] \left[\begin{array}{c} \underline{\xi}_{s-} \\ \hline \underline{\xi}_s(d) \end{array}\right] + \left[\begin{array}{c} \underline{\nu}_{s-} \\ \hline \underline{\nu}_s(d) \end{array}\right]. \tag{72}$$

Now, by invoking the earlier assumptions that the elements of the matrix Γ_{s2} are mostly negligible and that all M (DC) elements of $\underline{\xi}(d)$ are equal if the object is entirely covered by all M projections, we obtain the following two equations

$$\underline{\psi}_{s-} \approx \Gamma_{s1} \underline{\xi}_{s-} + \underline{\nu}_{s-} \tag{73}$$

$$\frac{\mu M}{N} \approx cM^2 + \nu_{\oplus} \tag{74}$$

where $\nu_{\oplus} \sim N(0, M\lambda)$. From Equation 74, the maximum likelihood estimate of c is $\mu/(MN)$. This is the same as the value of c we had used earlier in the case of no noise (Equation 88). The MAP estimate of $\underline{\xi}_{s-}$, from Equation 73, is given by

$$\hat{\underline{\xi}}_{s-} = \arg\max_{\underline{\xi}_{s-}} [P(\underline{\xi}_{s-} | \underline{\psi}_{s-})] \tag{75}$$

$$= [P_{\xi_{s-}}^{-1} + \Gamma_{s1}^T R_{\nu_{s-}}^{-1} \Gamma_{s1}]^{-1} \Gamma_{s1}^T R_{\nu_{s-}}^{-1} \underline{\psi}_{s-} \tag{76}$$

where $R_{\nu_{s-}} = \lambda I_{M(N-1) \times M(N-1)}$, and $P_{\xi_{s-}}$ is the prior covariance of $\underline{\xi}_{s-} \sim N(\underline{0}, P_{\xi_{s-}})$. We assume $\underline{\xi}_{s-}$ to be uncorrelated (or, equivalently, $P_{\xi_{s-}}$ to be a diagonal matrix) with a geometrically decreasing variance from coarse to fine scales. Thus the diagonal elements of $P_{\xi_{s-}}$ are given by

$$E(\xi_{ksn}^T \xi_{ksn}) = 2^{-\rho(l-s)} \qquad \text{for } s = h, h+1, \ldots, l \tag{77}$$

where ρ is a regularization parameter. This implies that the projection data mostly influences the reconstruction of coarse scale features and the prior model influences the reconstruction of fine scale features. This is desired since the high frequencies (i.e. the fine scales) are mostly corrupted by noise. Equation 76 can now be simplified to (compare with Equation 60)

$$\hat{\underline{\xi}}_{s-} = A \underline{\psi}_{s-} + \underline{b} \tag{78}$$

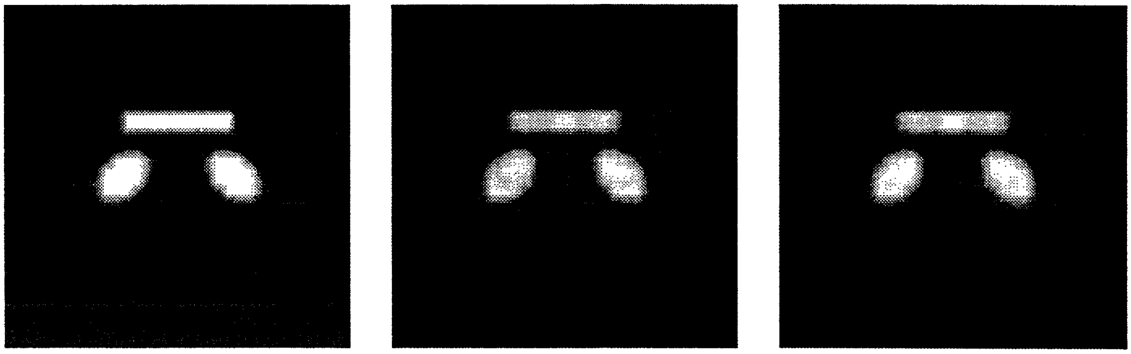

Figure 10: Left: A 32×32 Phantom. Middle: CBP reconstruction using a ramp filter and $M = N = 32$. Right: Complete multiscale reconstruction.

where

$$A = (\Gamma_{s1}^2 + \lambda P_{\xi_s,-}^{-1})^{-1}\Gamma_{s1} \tag{79}$$

and

$$\underline{b} = \underline{0}. \tag{80}$$

Thus the only change in the reconstruction algorithm from the noiseless case is that different expressions for A and $\underline{b}$, given by Equations 79 and 80 respectively, are to be used now for reconstructions from noisy data, with λ and ρ serving as regularization parameters. An increased regularization results by increasing λ for a fixed ρ, or by increasing ρ for a fixed λ.

5 Results

5.1 Demonstration of the reconstruction method

Figure 10 shows a phantom along with the CBP and the complete multiscale reconstruction. The size of the phantom is 32×32 and the imaging geometry is defined by $M = N = 32$. We have used a ramp filter (i.e. we have not introduced any regularization) in the CBP reconstruction. Thus, for this complete data case, the CBP and the multiscale reconstructions should be similar. This is precisely what is seen in Fig 10 and confirmed in Fig 11 which shows a section through the reconstructions[6]. It is observed that the maximum absolute difference in the reconstructed pixel intensities is of the order of 10^{-5} when different wavelets are used to reconstruct this same phantom.

In Figure 12 we show the reconstruction of a 32×32 phantom from projection data collected using $M = N = 32$. The D_3 wavelet is used for multiscale reconstruction. Figure 12 is the *combined scale* reconstruction where the reconstruction at a particular scale includes the contributions from

---

[6] The discrepancy between the CBP and the multiscale reconstructions near the edges is due to the fact that we are reconstructing on a circle in case of the latter rather than on the entire square field-of-view as in the former.

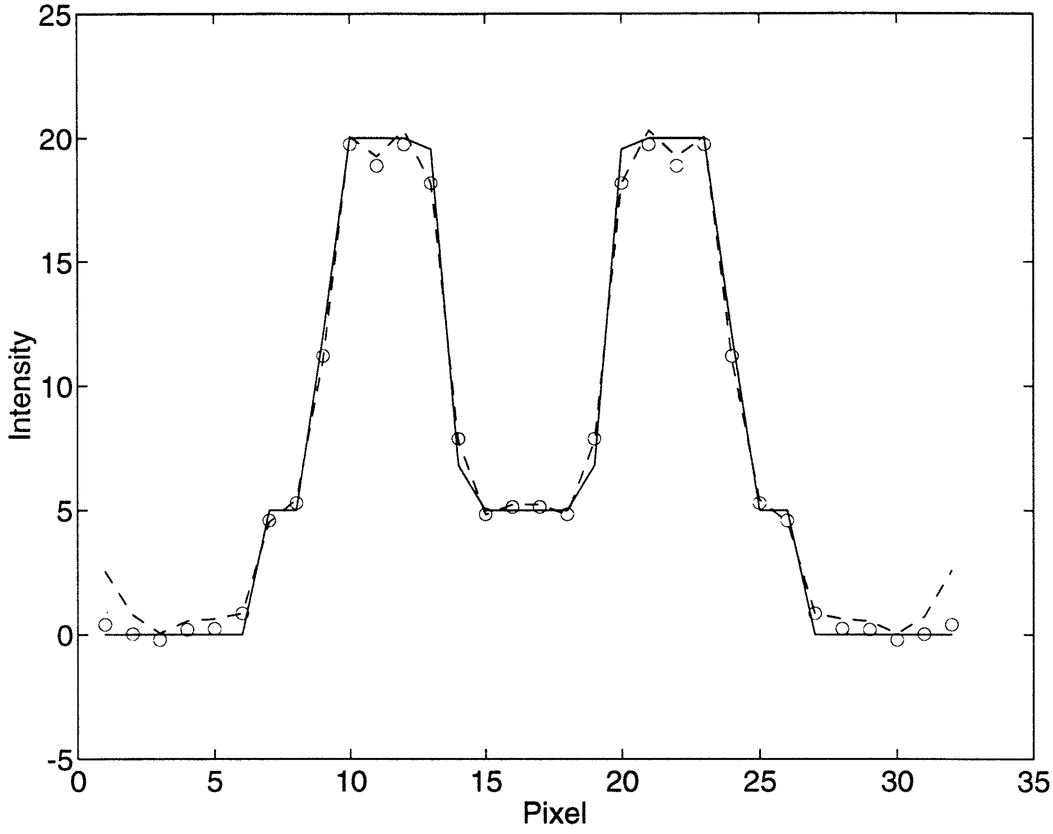

Figure 11: A horizontal section through the phantom (solid line) and the CBP (circles) and multiscale (broken line) reconstructions.

all scales coarser to and including that scale. In Figure 13 (the *separate scale* reconstruction) we show the individual contributions at different scales.

5.2 Reconstruction of fine scale features by approximating Γ_{s1} as an identity matrix

In Figure 14, we show the CBP reconstruction, the complete multiscale reconstruction and the finest scale contribution from the reconstruction of a 32×32 phantom using the Haar basis. We use only the diagonal elements of matrix Γ_{s1} for reconstruction and assume that they are all equal to 1. It can be shown with relative ease that the complete multiscale reconstruction in this case is the same as simple back-projection reconstruction having a $1/r$ blurring. We can see, from the finest scale contribution, that if the goal is edge reconstruction, it is enough to approximate Γ_{s1} by an identity matrix. This reduces the computational complexity enormously. The edge reconstruction, in the multiscale framework, only involves the 1-D Haar transform of the strip integral data and subsequent back-projection of fine scale coefficients.

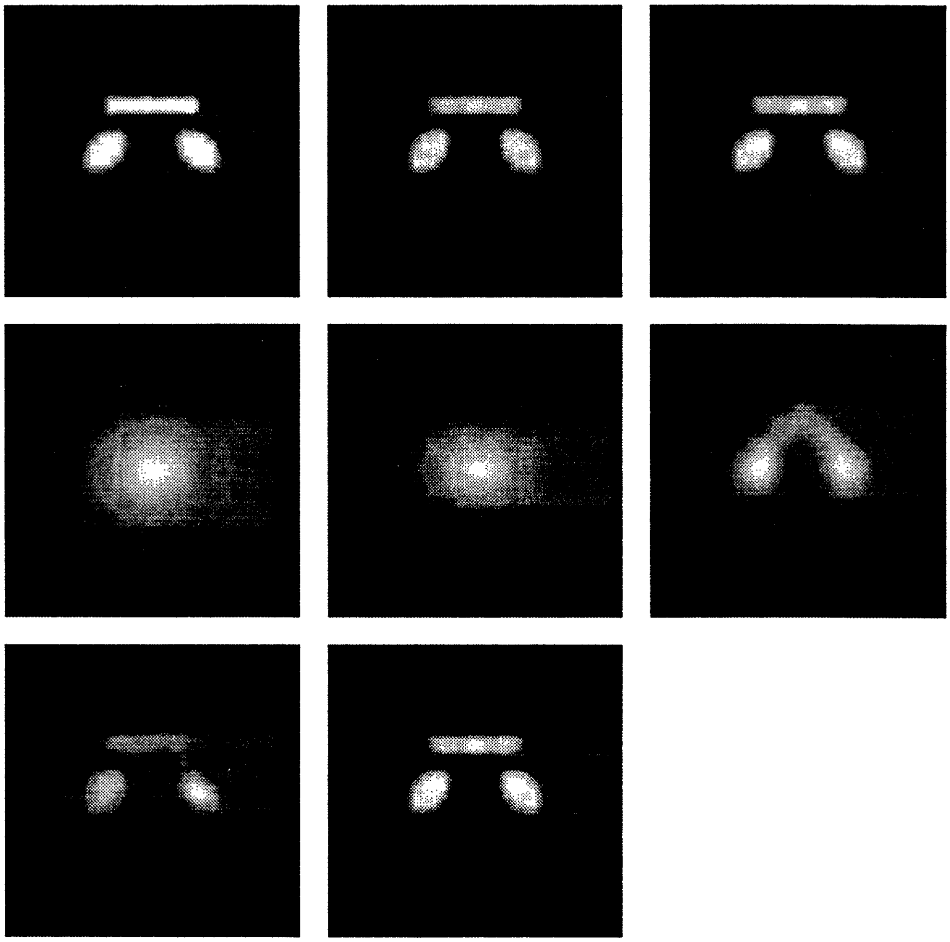

Figure 12: Combined scale reconstructions, using the D_3 wavelet, of a 32×32 phantom with $M = N = 32$. Top row, left: Phantom. Top row, middle: CBP reconstruction using a ramp filter. Top row, right: Multiscale reconstruction. Reconstruction including contributions from all scales at and coarser to: Middle row, left: Scale 1. Middle row, middle: Scale 2. Middle row, right: Scale 3. Bottom row, left: Scale 4. Bottom row, middle: Scale 5. The reconstructions in top row, right and bottom row, middle are identical.

5.3 Reconstruction from incomplete data

In Fig 15 we show a 32×32 phantom reconstructed using the Haar wavelet and $M = 5$ and $N = 32$, i.e. using 5 uniformly spaced angular projections, each containing 32 parallel strips. This is the incomplete data case and hence the multiscale reconstruction is expected to be free of the many artifacts which arise in the CBP reconstruction due to the space-invariance assumption. This is exactly what is seen in the figure. This figure also indicates the resolution-accuracy tradeoff. The reconstruction at Scale 3 (middle row, right, in the figure) does not enable one to distinguish between the two circles, but the reconstruction has very few artifacts. The distinguishability increases, accompanied by an increase in the artifacts, at Scale 5 (i.e. full multiscale reconstruction). Fig 16

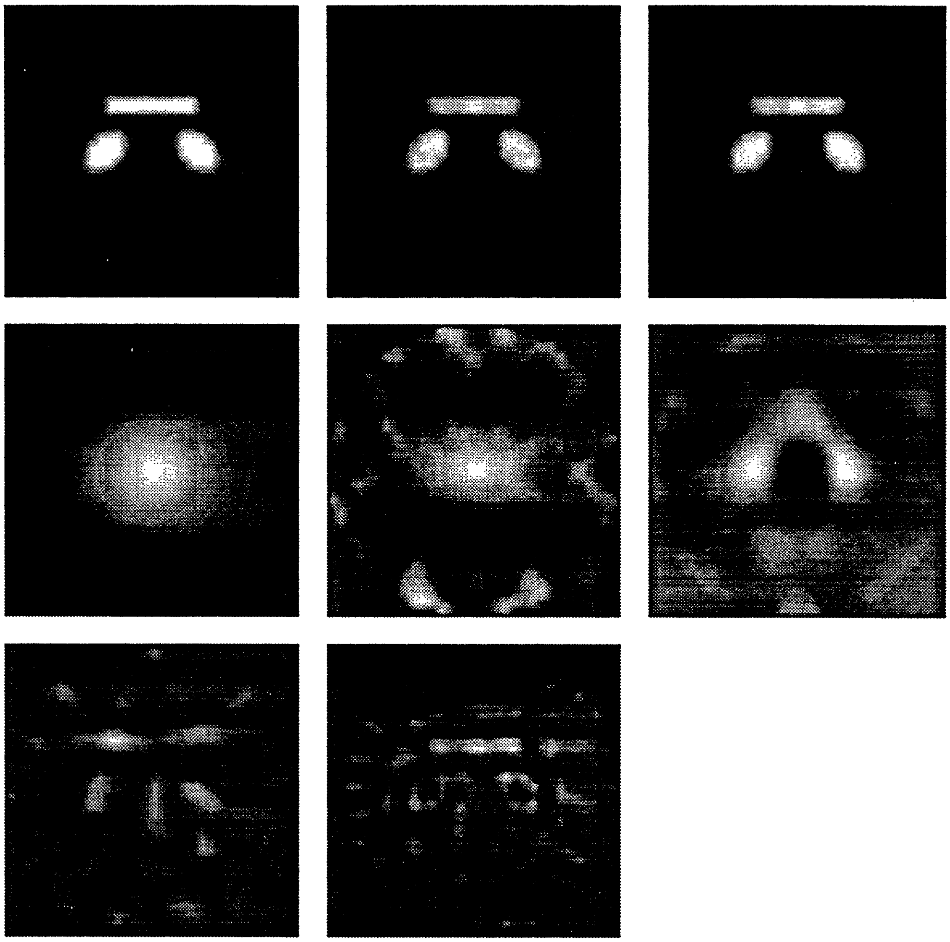

Figure 13: Separate scale reconstructions, using the D_3 wavelet, of a 32×32 phantom with $M = N = 32$. Top row, left: Phantom. Top row, middle: CBP reconstruction using a ramp filter. Top row, right: Multiscale reconstruction. Reconstruction including contributions from all scales at and coarser to: Middle row, left: Scale 1. Middle row, middle: Scale 2. Middle row, right: Scale 3. Bottom row, left: Scale 4. Bottom row, middle: Scale 5.

shows another example of the incomplete data case. The parameters here are the same as in Fig 15 and the same suppression of artifacts is seen.

5.4 Reconstruction from noisy data

Figure 17 shows a phantom along with the unregularized and regularized (MAP) complete multiscale reconstructions after adding 5 dB noise to the projection data. The size of the phantom is 32×32 and the imaging geometry is defined by $M = N = 32$. We have used the D_3 wavelet for multiscale reconstructions. The two regularized reconstructions correspond to regularization

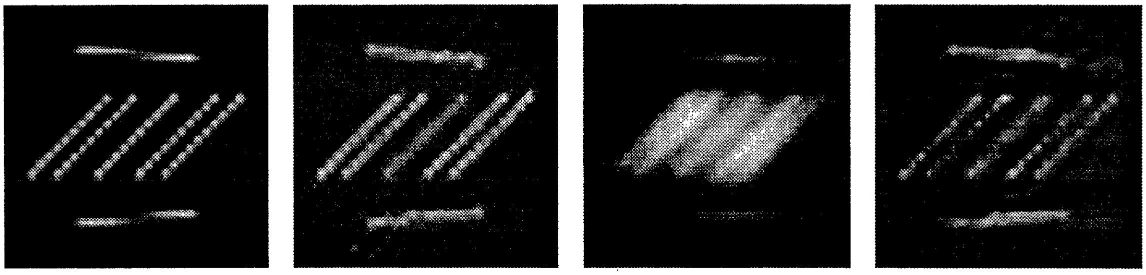

Figure 14: From left (a) 32×32 Phantom, (b) CBP reconstruction with $M = N = 32$ (c) Complete multiscale reconstruction, and (d) The finest scale contribution.

parameters $\lambda = 1$, $\rho = 0.5$ and $\lambda = \rho = 1$ respectively. Figure 18 shows a section through the reconstructions. From Figures 17 and 18 we see that, as is expected, an increased regularization results when the value of ρ is increased from 0.5 to 1, keeping λ constant at 1.

6 Conclusions

We have used the natural pixel object representation, where the object is expanded in the same basis functions along which the strip integral data is collected, as the starting point of our multiscale reconstruction method. In the natural pixel representation, the natural pixels (i.e. the expansion coefficients) and the strip integral data are related by the system matrix G. We decompose the natural pixels and the strip integral data in a multiscale basis so that they are related by a new system matrix Γ_θ which is sparse and, in addition, has a symmetric block-Toeplitz structure if the M angular projections are uniform between 0 and 180^0. Fast inversion algorithms exist for these matrices. For the incomplete data case, the multiscale reconstruction is relatively free of the many artifacts that plague the CBP reconstruction. We have shown, through examples, that for an ill-posed reconstruction problem, some regularization can be achieved by only combining coarser scale reconstructions instead of reconstructions at all the scales. For noisy data problems, we have specialized our multiscale reconstruction method to yield MAP multiscale reconstruction estimates corresponding to a chosen prior on the multiscale object coefficients. We have also shown that a fast method of detecting fine scale features, like edges and boundaries, in an object is by taking the Haar transform of the projection data and subsequently back-projecting the fine scale coefficients.

Currently, we are concentrating on regularizing ill-posed reconstruction problems by incorporating different stochastic priors in our multiscale reconstruction method. We use the multiscale framework to construct regularizing tree-based models in scale reflecting stochastic prior information about the object. Since fast algorithms exist for performing estimation on such multiscale trees (i.e. scale-recursive estimation algorithms which are a generalization of the Rauch-Tung-Striebel optimal smoothing algorithm) [14], our multiscale reconstruction method enables us to tackle ill-posed reconstruction problems at a speed much faster than existing methods. In addition, our technique provides object estimates at multiple scales along with corresponding error covariance information. This information is essential for assessing the resolution-accuracy tradeoff and determining an

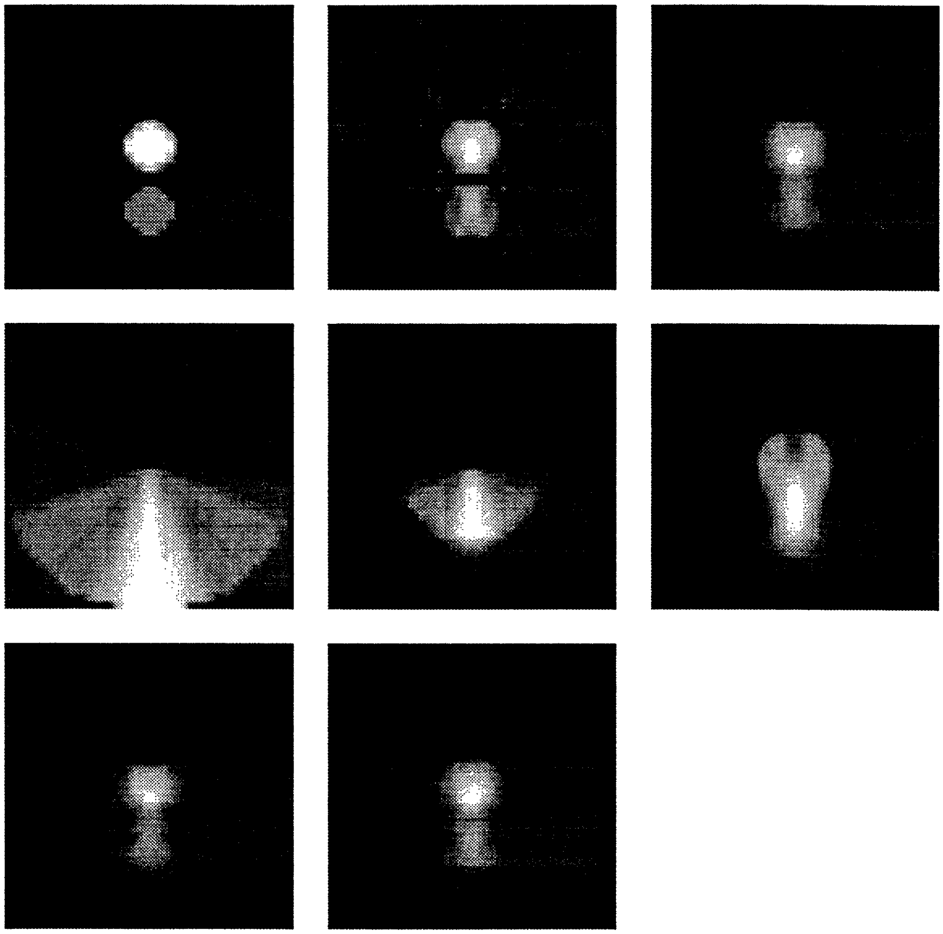

Figure 15: Combined scale reconstructions, using the Haar wavelet, of a 32 × 32 phantom with $M = 5$ and $N = 32$. Top row, left: Phantom. Top row, middle: CBP reconstruction using a ramp filter. Top row, right: Multiscale reconstruction. Reconstruction including contributions from all scales at and coarser to: Middle row, left: Scale 1. Middle row, middle: Scale 2. Middle row, right: Scale 3. Bottom row, left: Scale 4. Bottom row, middle: Scale 5. The reconstructions in top row, right and bottom row, middle are identical.

optimal scale for reconstruction of each portion of the object.

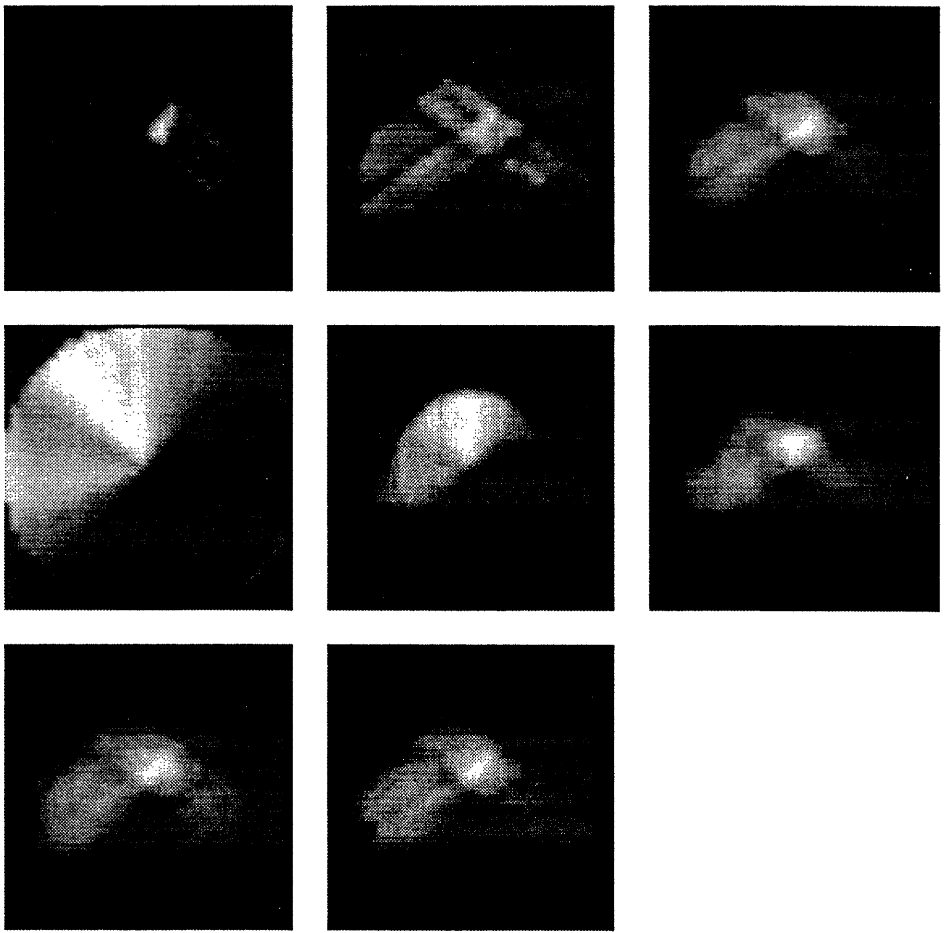

Figure 16: Combined scale reconstructions, using the Haar wavelet, of a 32 × 32 phantom with $M = 5$ and $N = 32$. Top row, left: Phantom. Top row, middle: CBP reconstruction using a ramp filter. Top row, right: Multiscale reconstruction. Reconstruction including contributions from all scales at and coarser to: Middle row, left: Scale 1. Middle row, middle: Scale 2. Middle row, right: Scale 3. Bottom row, left: Scale 4. Bottom row, middle: Scale 5. The reconstructions in top row, right and bottom row, middle are identical.

Appendices

Appendix 1: The matrix Γ_{sd} is circulant

Γ_{sd} has the form

$$\begin{bmatrix} <\underline{\Phi}_{1d1}, \underline{\Phi}_{1d1}> & <\underline{\Phi}_{1d1}, \underline{\Phi}_{2d1}> & <\underline{\Phi}_{1d1}, \underline{\Phi}_{3d1}> & \cdots & <\underline{\Phi}_{1d1}, \underline{\Phi}_{Md1}> \\ <\underline{\Phi}_{2d1}, \underline{\Phi}_{1d1}> & <\underline{\Phi}_{2d1}, \underline{\Phi}_{2d1}> & <\underline{\Phi}_{2d1}, \underline{\Phi}_{3d1}> & \cdots & <\underline{\Phi}_{2d1}, \underline{\Phi}_{Md1}> \\ \vdots & \vdots & \vdots & \vdots & \vdots \\ <\underline{\Phi}_{Md1}, \underline{\Phi}_{1d1}> & <\underline{\Phi}_{Md1}, \underline{\Phi}_{2d1}> & <\underline{\Phi}_{Md1}, \underline{\Phi}_{3d1}> & \cdots & <\underline{\Phi}_{Md1}, \underline{\Phi}_{Md1}> \end{bmatrix} \tag{81}$$

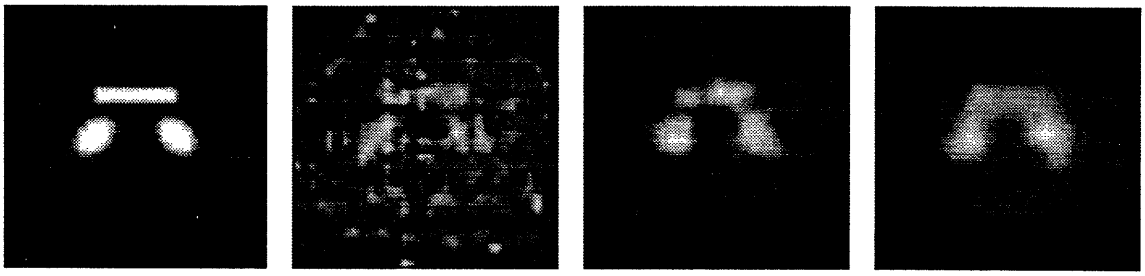

Figure 17: From left (a) 32×32 Phantom, (b) Unregularized complete multiscale reconstruction with $M = N = 32$ and 5 dB noise, (c) Regularized complete multiscale reconstruction with $\lambda = 1$ and $\rho = 0.5$, and (d) Regularized complete multiscale reconstruction with $\lambda = 1$ and $\rho = 1$.

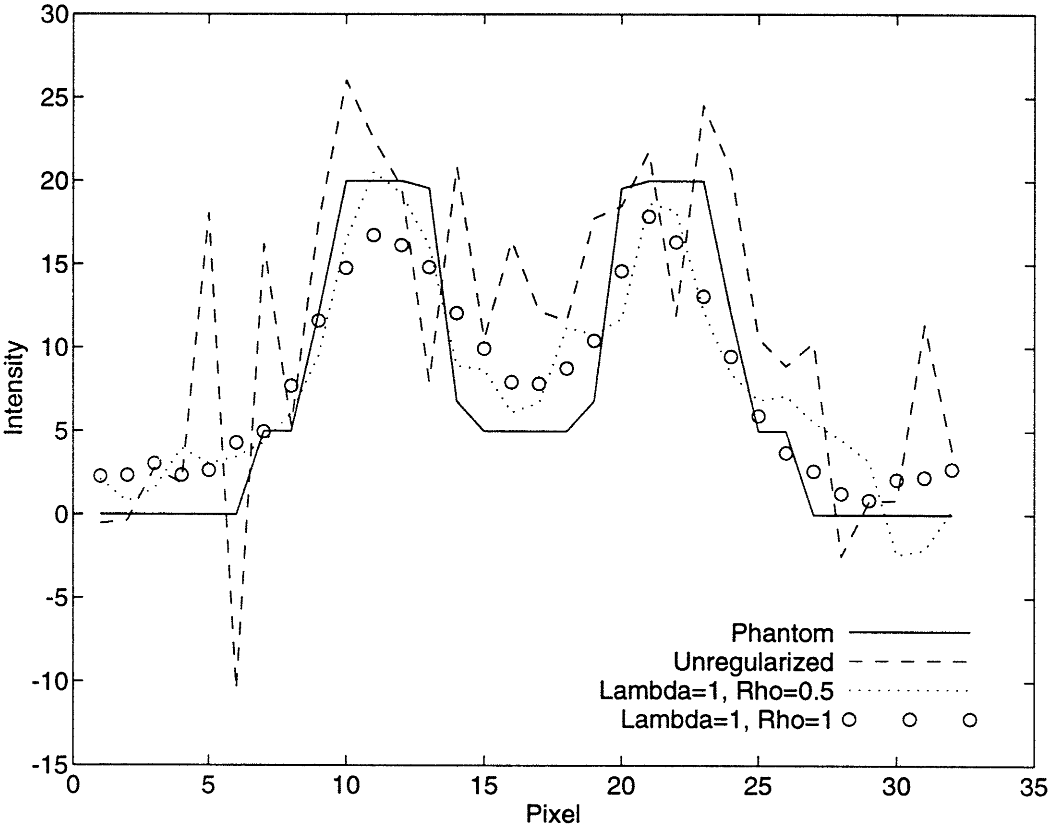

Figure 18: A horizontal section through the phantom (solid line) and the various reconstructions of the previous figure.

where $< e, g >$ refers to the inner product or, equivalently, the area of intersection of e and g. Clearly, since $< \underline{\Phi}_{id1}, \underline{\Phi}_{jd1} >=< \underline{\Phi}_{jd1}, \underline{\Phi}_{id1} >$, Γ_{sd} is symmetric. Also, all $< \underline{\Phi}_{id1}, \underline{\Phi}_{id1} >$, $i = 1, 2, \ldots, M$ are equal to 1 because of our usage of normalized basis functions. Further, because of our assumption of uniformly spaced projection angles, $< \underline{\Phi}_{id1}, \underline{\Phi}_{jd1} >$ is a function of only $|(i)\mathrm{mod}(M) - (j)\mathrm{mod}(M)|$. This results in a symmetric circulant Γ_{sd}.

Let the constant row sum of Γ_{sd} be α. Then

$$\alpha = \sum_{i=1}^{M} < \underline{\Phi}_{1d1}, \underline{\Phi}_{id1} > . \tag{82}$$

It can be shown, by elementary geometry, that

$$< \underline{\Phi}_{1d1}, \underline{\Phi}_{id1} >= \begin{cases} \dfrac{\sin\theta + \cos\theta - 1}{\sin\theta\cos\theta} & \text{for } 0 < \theta < 90^0, \\ 1 & \text{for } \theta = 0,\ 90^0, \\ < \underline{\Phi}_{1d1}, \underline{\Phi}_{(M+2-i)d1} > & \text{for } i = 1, 2, \ldots, M/2 \text{ if } M \text{ is even, and} \\ & \text{for } i = 1, 2, \ldots, (M+1)/2 \text{ if } M \text{ is odd.} \end{cases} \tag{83}$$

From Equation 83, it can be shown that $< \underline{\Phi}_{1d1}, \underline{\Phi}_{id1} >$ achieves a minimum value equal to $2(\sqrt{2} - 1) = 0.83$ when i corresponds to a projection at 45^0 or 135^0. The maximum value of $< \underline{\Phi}_{1d1}, \underline{\Phi}_{id1} >$ is 1 when i corresponds to projections at 0^0 or 90^0. For most applications, it is enough to approximate the row sum of Γ_{sd}, α, by M. For $M = 16$, α has a value 14.2, and for $M = 32$ a value of 28.3.

Appendix 2: Details of the NP based multiscale reconstruction method

By adding the last M equations in the matrix partitioned equation (56), we get

$$\left[\begin{array}{c} \underline{\psi}_{s-} \\ \hline \frac{\mu M}{N} \end{array}\right] = \left[\begin{array}{c|c} \Gamma_{s1} & \underline{v} \\ \hline \underline{v}^T & \alpha M \end{array}\right] \left[\begin{array}{c} \underline{\xi}_{s-} \\ \hline c \end{array}\right] . \tag{84}$$

Now, by applying the matrix inversion lemma to above [13],

$$\underline{\xi}_{s-} = \Gamma_{s1}^{-1} \underline{\psi}_{s-} - \Gamma_{s1}^{-1} \underline{v} \left[\frac{\underline{v}^T \Gamma_{s1}^{-1} \underline{\psi}_{s-} - \frac{\mu M}{N}}{\underline{v}^T \Gamma_{s1}^{-1} \underline{v} - \alpha M} \right] . \tag{85}$$

Also, from Equation 84,

$$\frac{\mu M}{N} = \underline{v}^T \underline{\xi}_{s-} + \alpha M c. \tag{86}$$

Now the elements of $\underline{v}$ are the row sums of Γ_{s2}^T. Since the elements of Γ_{s2} are the areas of intersection of basis functions $\{\underline{\Phi}_{kd1};\ k = 1, \ldots, M\}$ with $\{\underline{\Phi}_{ksn};\ k = 1, \ldots, M;\ s = h, h+1, \ldots, l;\ n = 1, \ldots, n_s\}$, they are mostly negligible[7]. Thus we can approximate

$$\frac{\mu M}{N} \approx \alpha M c \tag{87}$$

---

[7] Appendix 3 demonstrates the validity of this assumption for the Haar case. For arbitrary compactly supported Daubechies wavelets, this assumption is seen to be valid even though it is difficult to calculate numerical bounds as is done in the Haar case.

or

$$c \approx \frac{\mu}{\alpha N} \approx \frac{\mu}{MN} \tag{88}$$

using the approximation $\alpha \approx M$ (refer to Appendix 1).

Thus the multiscale reconstruction reduces to calculating and back-projecting

$$\underline{\xi}_s = \begin{bmatrix} \underline{\xi}_{s-} \\ \frac{\mu}{MN}\underline{1}_M \end{bmatrix} \tag{89}$$

where $\underline{\xi}_{s-}$ is given by Equation 85. Let $\Phi_s = P\Phi$, where Φ is the matrix containing the multiscale basis functions arranged according to projection angles and P is the same permutation matrix as discussed earlier. The multiscale reconstruction is then given by

$$\underline{\hat{f}} = \Phi_s^T \underline{\xi}_s = \begin{bmatrix} \Phi_{s-}^T & \Phi_{sd}^T \end{bmatrix} \begin{bmatrix} \underline{\xi}_{s-} \\ \frac{\mu}{MN}\underline{1}_M \end{bmatrix} = \Phi_{s-}^T \underline{\xi}_{s-} + \frac{\mu}{MN}\Phi_{sd}^T \underline{1}_M. \tag{90}$$

Since we assume that the object is fully covered by all M projections, we are only interested in reconstructing the intersection of the field-of-views of the M projections. Thus

$$\begin{aligned} \underline{\hat{f}} &\approx \Phi_{s-}^T \underline{\xi}_{s-} + \frac{\mu}{MN}\frac{M}{N}\underline{1}_{N^2} \\ &= \Phi_{s-}^T \underline{\xi}_{s-} + \frac{\mu}{N^2}\underline{1}_{N^2}. \end{aligned} \tag{91}$$

Appendix 3: The elements of the matrix Γ_{s2} are mostly negligible - demonstration for the Haar case

The elements of Γ_{s2} are the areas of intersection of basis functions $\{\underline{\Phi}_{kd1};\ \ k = 1, \ldots, M\}$ with $\{\underline{\Phi}_{ksn};\ \ k = 1, \ldots, M;\ \ s = h, h+1, \ldots, l;\ \ n = 1, \ldots, n_s\}$. The maximum absolute value in Γ_{s2} corresponds to $< \underline{\Phi}_{k_1 d1}, \underline{\Phi}_{k_2 (s=l-1)1} >$ (or $< \underline{\Phi}_{k_1 d1}, \underline{\Phi}_{k_2 (s=l-1)n_s} >$), where projections k_1 and k_2 are separated by 45^0. This value is equal to $5\sqrt{2}/8 - 1 = 0.12$. But the majority of the terms in Γ_{s2} correspond to the areas of intersection with fine scale basis functions, which are negligible. As an example, for fine scales $s = h$ and $h+1$, the absolute value of $< \underline{\Phi}_{id1}, \underline{\Phi}_{js*} >$ is bounded by

$$(2^{(l-s)/2})(\frac{z}{4})\frac{(\sin\theta + \cos\theta - 1)}{(\sin\theta\cos\theta)}\left[1 - \sqrt{1 + \frac{8z}{(\sin\theta + \cos\theta - 1)} + \frac{16z^2}{(\sin\theta + \cos\theta - 1)^2}}\right] \tag{92}$$

where

$$z = (0.5)^{l+1-s} \tag{93}$$

and projections i and j are separated by angle θ with $0 < \theta < 90^0$. It is enough to consider $0 < \theta < 90^0$, as for $90^0 < \theta < 180^0$ the same bounds apply. For $\theta = 0$ or 90^0, the areas of intersection $< \underline{\Phi}_{id1}, \underline{\Phi}_{js*} >$ are identically zero.

Thus, as an example, for $\theta = 11.25^0$, $< \underline{\Phi}_{id1}, \underline{\Phi}_{js*} >$ has a maximum absolute value of 0.02 for $s = h$ and 0.05 for $s = h+1$. For $\theta = 45^0$, these values are 0.008 and 0.02 respectively.

Appendix 4: Justification for odd M

In case of odd M, $[\Gamma_{s2} \ \ \Gamma_{sd}]$ has full row rank. Now

$$\begin{aligned} \frac{\mu}{N}\underline{1}_M &= \begin{bmatrix} \Gamma_{s2} & \Gamma_{sd} \end{bmatrix} \begin{bmatrix} \underline{\xi}_{s-} \\ \underline{\xi}_s(d) \end{bmatrix} & (94) \\ &= \Gamma_{s2}\underline{\xi}_{s-} + \Gamma_{sd}\underline{\xi}_s(d). & (95) \end{aligned}$$

Invoking the earlier assumption that the elements of Γ_{s2} are mostly negligible

$$\frac{\mu}{N}\underline{1}_M \approx \Gamma_{sd}\underline{\xi}_s(d) \tag{96}$$

or

$$\underline{\xi}_s(d) \approx \frac{\mu}{N}\Gamma_{sd}^{-1}\underline{1}_M = \frac{\mu}{N}\underline{r} \tag{97}$$

where $\underline{r}$ is a vector containing the row sums of Γ_{sd}^{-1}. Now, as proved in Appendix 5, a circulant matrix and it's inverse both have constant row sums. Moreover, the row sum of the inverse is the reciprocal of the row sum of the matrix itself. Since Γ_{sd} is circular and it's row sum $\alpha \approx M$, all M elements of $\underline{r}$ are approximately equal to $1/M$. Hence

$$\begin{aligned} \underline{\xi}_s(d) &\approx \frac{\mu}{MN}\underline{1}_M & (98) \\ &= c\underline{1}_M. & (99) \end{aligned}$$

Thus all M elements of $\underline{\xi}_s(d)$ are equal for odd M.

Appendix 5

Claim: The inverse of a circulant matrix C, if it exists, has constant row sums which are reciprocal of the constant row sum of C.

Proof: Consider a $M \times M$ circulant matrix C. We can always diagonalize C as follows [15]

$$C = F^*DF \tag{100}$$

with

$$F = F^T = \frac{1}{\sqrt{M}} \begin{bmatrix} 1 & 1 & \dots & 1 \\ 1 & \exp[-j(2\pi/M)] & \dots & \exp[-j(2\pi/M)(M-1)] \\ \vdots & \vdots & \vdots & \vdots \\ 1 & \exp[-j(2\pi/M)(M-1)] & \dots & \exp[-j(2\pi/M)(M-1)^2] \end{bmatrix} \tag{101}$$

where * denotes complex conjugation, $F^*F = FF^* = I$ and $D = \text{diag}(d_1, d_2, \dots, d_M)$. Now

$$C\underline{1}_M = F^*DF\underline{1}_M = F^* \times \text{diag}(d_1, d_2, \dots, d_M) \times \begin{bmatrix} \sqrt{M} \\ 0 \\ \vdots \\ 0 \end{bmatrix} \tag{102}$$

since

$$\sum_{i=0}^{M-1} \exp\left[\pm j(2\pi/M)ki\right] = 0 \qquad \text{for } k \text{ an integer and } 1 \leq k \leq M-1. \tag{103}$$

Hence

$$C\underline{1}_M = \sqrt{M} d_1 F^* \begin{bmatrix} 1 \\ 0 \\ \vdots \\ 0 \end{bmatrix} = d_1 \underline{1}_M. \tag{104}$$

Now

$$C^{-1} = F^{-1} D^{-1} (F^*)^{-1} = F^* D^{-1} F. \tag{105}$$

Hence

$$C^{-1}\underline{1}_M = \frac{1}{d_1}\sqrt{M} F^* \begin{bmatrix} 1 \\ 0 \\ \vdots \\ 0 \end{bmatrix} = \frac{1}{d_1}\underline{1}_M. \tag{106}$$

Thus, from Equations 104 and 106, the proof is complete.

Appendix 6: Summary of notations

Tables 1 and 2 summarize the notations developed for the conventional and the multiscale reconstruction techniques, respectively.

References

[1] A. C. Kak and M. Slaney, *Principles of Computerized Tomographic Imaging*, IEEE Press, 1988.

[2] K. M. Hanson, "Bayesian and Related Methods in Image Reconstruction from Incomplete Data," in *Image Recovery Theory and Application*, Edited by H. Stark, Academic Press, 1987.

[3] K. M. Hanson, "Detectability in Computed Tomography Images," *Medical Physics*, Vol. 6, September/October 1979, pp. 441-451.

[4] N. Srinivasa, K. R. Ramakrishnan, and K. Rajgopal, "Detection of Edges from Projections," *IEEE Transactions on Medical Imaging*, Vol. 11, No. 1, March 1992, pp. 76-80.

[5] M. H. Buonocore, W. R. Brody and A. Macovski, "A Natural Pixel Decomposition for Two-Dimensional Image Reconstruction," *IEEE Transactions on Biomedical Engineering*, Vol. BME-28, No. 2, February 1981, pp. 69-78.

[6] M. H. Buonocore, W. R. Brody and A. Macovski, "Fast Minimum Variance Estimator for Limited Angle CT Image Reconstruction," *Medical Physics*, Vol. 8, No. 5, September/October 1981, pp. 695-702.

Table 1: Notations developed for conventional reconstruction techniques.

Notation	**Explanation**
M	Number of angular projections.
N	Number of strip integrals in each angular projection.
$\underline{f}$	The discretized object, defined on a $p \times p$ square grid. We set $p = N$.
$\underline{\hat{f}}$	The reconstructed object.
$\underline{y}(k)$	Projection data set at angle k, $k = 1, \ldots, M$. $\underline{y}(k) = [y_{k1}\, y_{k2} \,\cdots\, y_{kN}]^T$.
$\underline{y}$	Full projection data set. $\underline{y} = [\underline{y}^T(1)\, \underline{y}^T(2) \ldots \underline{y}^T(M)]^T$.
$\underline{x}(k)$	Object coefficient set at angle k, $k = 1, \ldots, M$. $\underline{x}(k) = [x_{k1}\, x_{k2} \,\cdots\, x_{kN}]^T$.
$\underline{x}$	Full object coefficient set. $\underline{x} = [\underline{x}^T(1)\, \underline{x}^T(2) \ldots \underline{x}^T(M)]^T$.
ϕ	The projection operator, $\underline{y} = \phi \underline{f}$.
ϕ^T	The back-projection operator, $\underline{\hat{f}} = \phi^T \underline{x}$.
T_a	The matrix representing the CBP ramp filtering operation for a projection data set at a particular angle. $\underline{x}(k) = T_a \underline{y}(k)$, $k = 1, \ldots, M$.
$I_{M \times M}$	The $M \times M$ identity matrix.
$\otimes$	The Kronecker product.
T	$T = I_{M \times M} \otimes T_a$, $\underline{x} = T\underline{y}$.
G	The NP input-output matrix, $\underline{y} = G\underline{x}$, $G = \phi\phi^T$.

[7] J. Llacer, "Theory of Imaging With a Very Limited Number of Projections," *IEEE Transactions on Nuclear Science*, Vol. NS-26, No. 1, February 1979, pp. 596-602.

[8] J. Llacer and J. D. Meng, "Matrix Based Image Reconstruction Methods for Tomography," *IEEE Transactions on Nuclear Science*, Vol. NS-32, No. 1, February 1985, pp. 855-864.

[9] J. Llacer, "Tomographic Image Reconstruction by Eigenvector Decomposition : It's Limitations and Areas of Applicability," *IEEE Transactions on Medical Imaging*, Vol. MI-1, No. 1, July 1982, pp. 34-42.

[10] I. Daubechies, *Ten Lectures on Wavelets*, S.I.A.M., 1992.

[11] N. H. Getz, "A Perfectly Invertible, Fast, and Complete Wavelet Transform for Finite Length Sequences: The Discrete Periodic Wavelet Transform," *Proceedings of the SPIE Annual Conference on Mathematical Imaging: Wavelet Applications in Signal and Image Processing*, San Diego, July 1993.

[12] G. H. Golub and C. F. Van Loan, *Matrix Computations*, The Johns Hopkins University Press, 1991, pp. 241-250.

[13] R. A. Horn and C. R. Johnson, *Matrix Analysis*, Cambridge University Press, 1991, pp. 18-19.

Table 2: Notations developed for multiscale reconstruction technique.

Notation	**Explanation**
ksn	Multiscale quantities are indexed by ksn. k is the angle of projection, $k = 1, \ldots, M$. s is the scale, $s = 1, 2, \ldots, 1 + \ln N / \ln 2\,;\ N = 2^i, i \in Z^+$. n is the shift within the scale, $n = 1, 2, \ldots, n_s\,;$ $n_s = N/2^s$ for $s = 1, 2, \ldots, \ln N/\ln 2$ and $n_s = 1$ for $s = 1 + \ln N/\ln 2$.
h	The finest scale, $s = 1 = h$.
l	The coarsest scale, $s = \ln N/\ln 2 = l$.
d	The DC component, $s = 1 + \ln N/\ln 2 = d$.
W_a	The matrix realization of the 1-D wavelet transform operation.
W	$W = I_{M \times M} \otimes W_a$.
$\underline{\psi}_\theta(k)$	The 1-D wavelet transform of $\underline{y}(k)$, $\underline{\psi}_\theta(k) = W_a \underline{y}(k)$.
$\underline{\psi}_\theta$	$\underline{\psi}_\theta = W\underline{y} = [\underline{\psi}_\theta^T(1)\, \underline{\psi}_\theta^T(2) \ldots \underline{\psi}_\theta^T(M)]^T$.
$\underline{\xi}_\theta(k)$	The 1-D wavelet transform of $\underline{x}(k)$, $\underline{\xi}_\theta(k) = W_a \underline{x}(k)$.
$\underline{\xi}_\theta$	$\underline{\xi}_\theta = W\underline{x} = [\underline{\xi}_\theta^T(1)\, \underline{\xi}_\theta^T(2) \ldots \underline{\xi}_\theta^T(M)]^T$.
Φ	The multiscale projection operator, $\underline{\psi}_\theta = \Phi \underline{f}$, $\Phi = W\phi$.
Φ^T	The multiscale back-projection operator, $\widehat{\underline{f}} = \Phi^T \underline{\xi}_\theta$.
Γ_θ	The multiscale input-output matrix arranged according to projection angles. $\underline{\psi}_\theta = \Gamma_\theta \underline{\xi}_\theta$, $\Gamma_\theta = \Phi\Phi^T$.
P	The orthogonal permutation matrix that changes projection angle ordering to scale ordering.
$\underline{\psi}_s(j)$	Contains all projection data at scale j. $\underline{\psi}_s(j) = [\underline{\psi}_\theta^T(1,j)\, \underline{\psi}_\theta^T(2,j) \ldots \underline{\psi}_\theta^T(M,j)]^T$.
$\underline{\psi}_s$	Contains projection data arranged according to scales. $\underline{\psi}_s = P\underline{\psi}_\theta = [\underline{\psi}_s^T(h)\, \underline{\psi}_s^T(h+1) \ldots \underline{\psi}_s^T(l)\, \underline{\psi}_s^T(d)]^T$.
$\underline{\xi}_s(j)$	Contains all object coefficients at scale j. $\underline{\xi}_s(j) = [\underline{\xi}_\theta^T(1,j)\, \underline{\xi}_\theta^T(2,j) \ldots \underline{\xi}_\theta^T(M,j)]^T$.
$\underline{\xi}_s$	Contains object coefficients arranged according to scales. $\underline{\xi}_s = P\underline{\xi}_\theta = [\underline{\xi}_s^T(h)\, \underline{\xi}_s^T(h+1) \ldots \underline{\xi}_s^T(l)\, \underline{\xi}_s^T(d)]^T$.
Γ_s	The multiscale input-output matrix arranged according to scales. $\underline{\psi}_s = \Gamma_s \underline{\xi}_s$, $\Gamma_s = P\Gamma_\theta P^T$.

[14] K. C. Chou, A. S. Willsky, and A. Benveniste, "Multiscale Recursive Estimation, Data Fusion, and Regularization," *To appear in IEEE Transactions on Automatic Control*, March 1994.

[15] P. J. Davis, *Circulant Matrices*, John Wiley & Sons, 1979, pp. 72-73.